FIELD MEASUREMENTS IN THE FERMILAB ELECTRON COOLING SOLENOID PROTOTYPE

A.C.Crawford, S.Nagaitsev and A.Shemyakin, Fermilab, P.O.Box 500, Batavia, IL 60510, U.S.A.
S. Seletsky, Univ. of Rochester, Rochester, NY 14627, U.S.A.
V. Tupikov, Budker INP, Lavrentieva 11, Novosibirsk 630090, Russia

1. INTRODUCTION

To increase the Tevatron luminosity, Fermilab is developing a high-energy electron cooling system [1] to cool 8.9-GeV/c antiprotons in the Recycler ring. The schematic layout of the Recycler Electron Cooling (REC) system is shown in Figure 1. Cooling of antiprotons requires a round electron beam with a small angular spread propagating through a cooling section with a kinetic energy of 4.3 MeV. To confine the electron beam tightly and to keep its transverse angles below 10^{-4} rad, the cooling section will be immersed into a solenoidal field of 50-150G. As part of the R&D effort, a cooling section prototype consisting of 9 modules (90% of the total length of a future section) was assembled and measured. This paper describes the technique of measuring and adjusting the magnetic field quality in the cooling section and presents preliminary results of solenoid prototype field measurements.

The design of the cooling section solenoid is discussed in Chapter 2. Chapter 3 describes details of a dedicated measurement system, capable of measuring small transverse field components, while the system's measurement errors are analyzed in Chapter 4. Chapter 5 contains measured field distributions of individual elements of the cooling section as well as an evaluation of the magnetic shielding efficiency. An algorithm of field adjustments for providing lowest possible electron trajectory perturbations is proposed in Chapter 6; also, this chapter shows the results of our first attempts of implementing the algorithm.

2. DESIGN OF THE COOLING SECTION SOLENOID

The 20 m cooling section consists of ten identical 2 m modules (Figure 2). The main magnetic element of the module is a solenoid creating a longitudinal magnetic field of 50 – 150 G. The solenoid is wound with a copper wire over an aluminum tube with fiberglass insulation between layers. The tubes with welded flanges were machined before winding with the accuracy of 0.15 mm to provide a better magnetic field quality. After winding the solenoid was inserted into another aluminum tube, and the assembly was filled with epoxy and heat cured. The solenoid is cooled by water flowing through four copper tube rings, spaced evenly along the solenoid and welded to the outer aluminum tube.

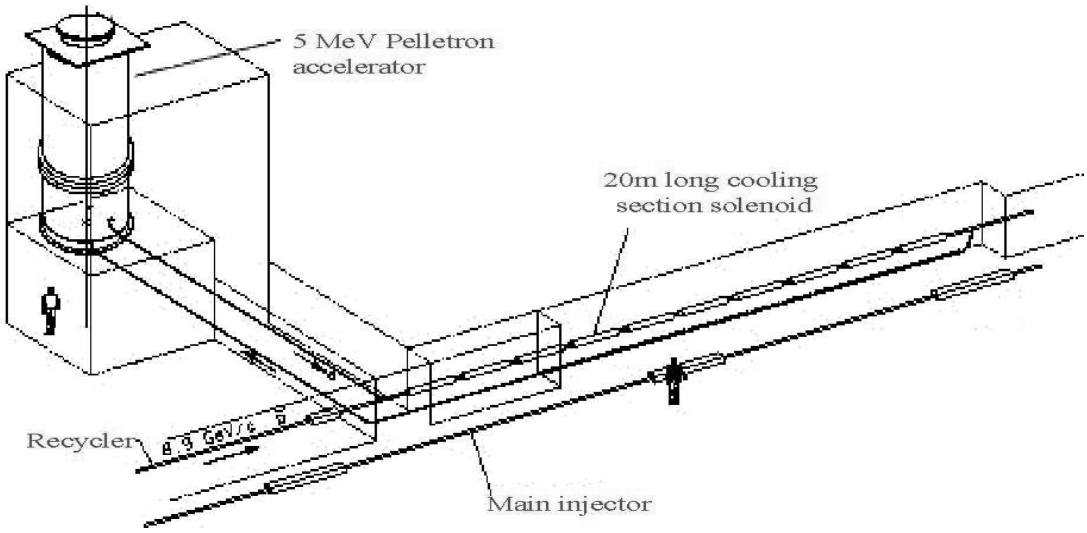

Figure 1 Schematic layout of Electron Cooling Experiment at Fermilab;

Table 1 Cooling section parameters

Parameter	***Value***
Total length of the cooling section	20 m
Number of modules	10
Gap length	8 cm
Module solenoid	
Length	1.882 m
Inner tube ID	14 cm
Outer tube OD	20 cm
Number of layers	6
Number of turns per layer	~1000
Copper wire size	Square AWG #13 (1.83 X 1.83 mm)
Resistance	17.7 Ω
Magnetic field at 1 A	40 G
Trim solenoid	
Length	3.5 cm
ID	14 cm
OD	20 cm
Total number of turns	13 turns x 22 layers
Copper wire gauge	AWG #16 (1.29 mm)
Resistance	2.5 Ω
Maximum magnetic field on axis at 1 A	49 G

Main dipole corrector	
Length	9.125" (23.28 cm)
Maximum current per coil	1 A
Maximum field	0.8 G
Copper trace width	0.015"
Spacing between traces	0.01"
Material	2- ounce copper on Kapton
Trim dipole corrector	
Length	1.4" (3.56 cm)
Maximum current per coil	1 A
Maximum field	1.0 G
Copper trace width	0.015"
Spacing between traces	0.01"
Material	2- ounce copper on Kapton
Shielding	
Material:	Permalloy 80 (IMP = 40,000 nominal)*
Material Thickness:	1 mm
Inner Radius of Layer #1	109 mm
Inner Radius of Layer #2	116 mm
Inner Radius of Layer #3	133 mm

* - See "Shielding" section for detail.

The solenoids are separated by instrumentation gaps, used for connecting beam diagnostics and vacuum pumps. To compensate detrimental effects of the field drop in these gaps, each module includes two short coils, the so-called trim solenoids, mounted on both sides of the solenoid. Transverse field components are adjusted by dipole coils made with a flexible circuit board technology. Each board carries four coils, which create fields in both transverse directions. Eight boards are wrapped around the solenoid (main correctors), and two, narrower ones, are positioned inside the trim solenoids, totaling in 20 independent channels per module.

To prevent beam perturbations by fringe fields of the ramping Main Injector, all elements of the cooling section are shielded by three layers of μ-metal

Some parameters of the cooling section and its components are listed in Table 1.

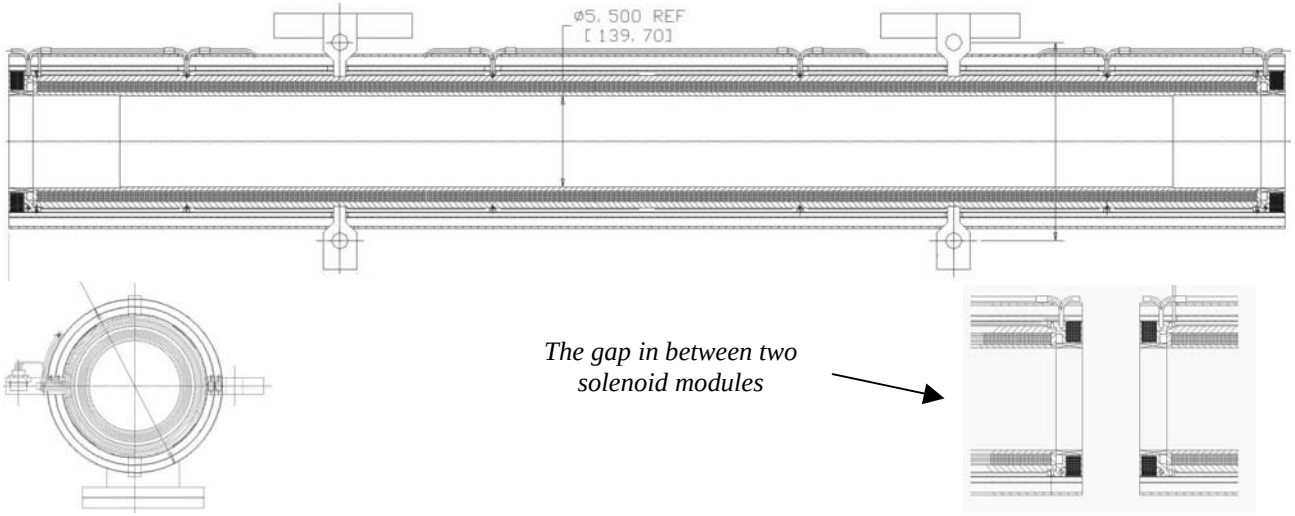

Figure 2 Drawing of cooling section solenoid

3. Measurement System

3.1 Principle of operation

The figure of merit for the cooling section magnetic field is the straightness of field lines. In the case of electron cooling (unlike, for example, NMR-tomography), requirements for transverse components are more stringent than those for the total magnetic field strength. An efficient way to measure the transverse components is to use a compass-based sensor. The method has been successfully employed in several laboratories (e.g. [2], [3]) at kG-range magnetic fields. Typically, such a sensor employs a gimbal-suspended magnetic-steel cylinder (compass) that is directed in a magnetic field along a field line. By measuring the angular position of the compass and the strength of the magnetic field *B* along the axis, one can determine the values of transverse components of the magnetic field. To find the angular position, a light beam is sent to a mirror, attached to the compass, and the angle between incident and the reflected beams is detected.

The method is shown to be capable of measuring relative values of the transverse components down to 10 μrad in fields of several kG [4]. On the other hand, its precision drops dramatically at lower fields. Figure 3 shows an error in the compass angular position after smooth increasing of the solenoid field from zero [5].

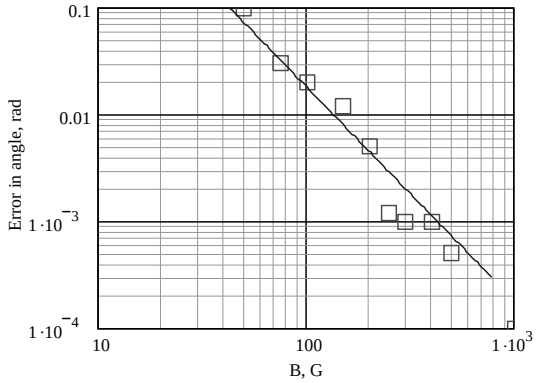

Figure 3 The error in a measured compass angular position after a smooth increase of the longitudinal magnetic field up to a value of B. *The solid line shows a fit to Eq. 3.2.*

The maximum angle α_{error} between the magnetic axis of the compass and the field line is determined by the friction in the gimbal:

$$\alpha_{error} = N_f /(M_c \cdot B), \qquad (3.1)$$

where N_f is a friction torque, M_c is the magnetic moment of the compass, and B is the magnetic field strength. The magnetic moment of a magnetic-steel cylinder is proportional to B, and

$$\alpha_{error} \propto 1/B^2. \qquad (3.2)$$

Hence, the use of a magnetic steel compass and a gimbal suspension makes the sensor imprecise at low magnetic fields. To accommodate the sensor for measurements at parameters of the Electron Cooling project, several major changes have been proposed by V. Parkhomchuck.

First, the steel cylinder was replaced by a *Nd-Fe-B* permanent magnet. It makes the compass magnetic moment practically independent on the value of the external field (for a hundred-Gauss range), and the error in (3.1) rises only as *1/B* at low fields. Estimations show that the magnetic moments for steel and permanent magnet cylinders become equal at the field strength of several kG.

Second, the compass is suspended by a 50 μm titanium wire instead of a gimbal to avoid friction. Generally speaking, the use of a wire at high fields can cause mechanical problems, when the compass passes regions with a nonuniform magnetic field, because of the force $\vec{F} = \nabla(\vec{M}_c \cdot \vec{B})$. However, at a hundred Gauss the force is tolerable and might result only in an increase of measurement errors in inhomogeneous field regions.

Third, instead of measuring the angle of a reflected light, a null method is used. Two pairs of dipole coils are mounted around the compass, and a feedback loop adjusts currents in the coils (Figure 4) until a full compensation of transverse components of the solenoid field is achieved. In this case, the compass mirror reflects the light (laser) beam onto the center of a position–sensitive device (in our case, it is a four-segment photodiode). After compensation, the values of currents in the coils are proportional to the solenoid transverse fields and are taken as a measure of these components. The scheme improves the precision of measurements and, by keeping the reflected laser beam near the solenoid axis, is very helpful for measuring of large field perturbations at distances up to 20 m.

The improvements were implemented in a sensor produced by Budker INP [6], which after some modifications, was used in the measurements of the cooling section solenoid. Below we are describing details of the measurement system.

3.2 System diagram

The schematic layout of the measuring system is shown in Figure 4. The cooling section optical axis is determined by a light beam, generated in a laser and shaped by an optical system. A mirror, attached to the compass reflects the beam to a 4-segmented photodiode. Using a pair of differential signals (for horizontal X and vertical Y directions) from photodiode segments, two identical electronic feedback systems generate currents in X and Y compensation dipole coils. The value of these currents is measured by digitizing of voltage drops on shunt resistors.

When solenoid transverse fields are compensated by the current in the coils, the reflected laser beam comes to the center of the photodiode and the system comes to the equilibrium. Coil currents multiplied by a normalizing coefficient are reported as values of the transverse components at the position of the compass.

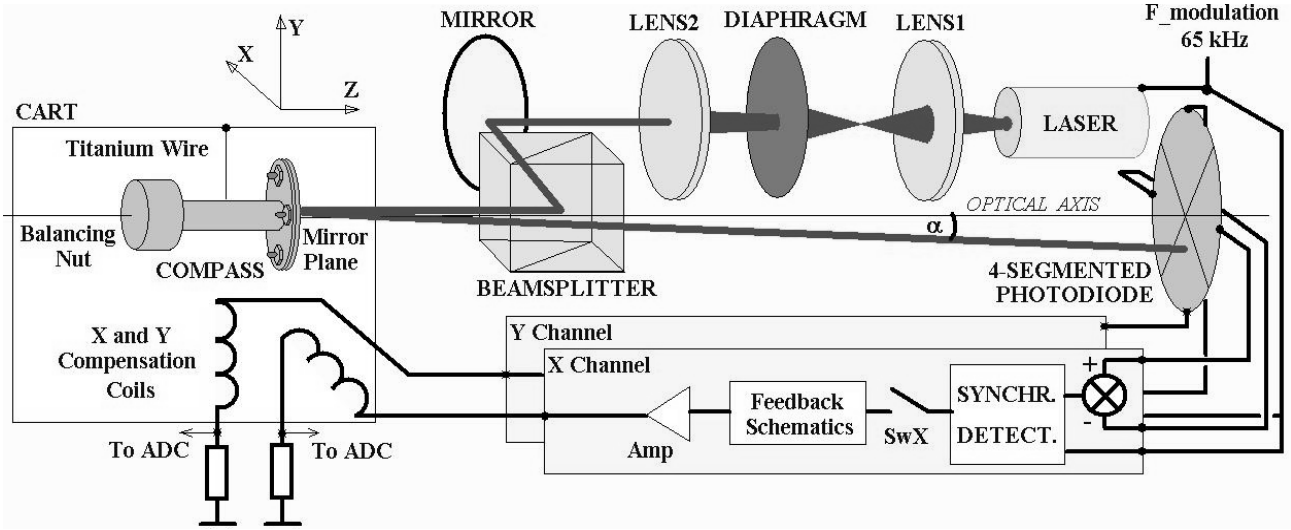

Figure 4 The block diagram of the magnetic measuring system

To exclude the daylight background of photodiode signal, the laser beam is modulated by a 65 kHz frequency. The modulation depth is close to 100%.

3.3 Compass Assembly

The compass assembly consists of a compass with an attached mirror and a holder where the compass hangs on a $\phi 50$ μm titanium wire.

The compass design is shown in Figure 5. Two cylindrical Nd-Fe-B permanent magnets of 10 mm length each are inserted into an aluminum field sensor body (1). A mirror is mounted on the adjuster (5) by four fixing screws (11) and attached to the main body by adjustment screws and nuts (7, 10). Four spring lock washers (6) between the adjuster and the main body provide capability of a fine adjustments of the mirror plane with respect to the magnetization vector of the compass. The achievable accuracy of such adjustments is better than 10^{-4} radians.

Position of the titanium wire in the compass body is determined by a 0.1 mm hole in the adjustment screw (8). The screw (9) has a thin slit in its center that clamps the wire when the fixing screws (3) are screwed in. The opposite end of the wire is held in the upper half of the holder (Figure 6) by an identical clamp. The vertical misbalance of the compass can be offset by adjusting the balancing nut (2). After mounting the compass inside the holder, the assembly is installed into a cart (see Section 3.5).

The compass holder design was optimized to improve damping of free compass oscillations. Here, unlike a gimbal scheme, friction in a suspension is low, and the main damping mechanism is probably the air friction. To enhance the effect, the size of the gap between the compass body and holder walls was minimized down to 1.5 mm. Also, some additional damping can be caused by eddy currents excited in the aluminum holder by magnetic fields of the oscillating compass. However, this effect might be rather weak at oscillation frequencies under 10 Hz, typical for our measurements at low magnetic fields.

To verify the importance of having a small gap, the free oscillation damping time in the regular compass assembly was compared with that measured when the lower half of the holder was removed (Figure 7). The oscillation were exited by a 10 mG jump of the transverse field induced by a dipole corrector and were measured as a synchronous detector signal with an open feedback loop. A two-fold increase of the damping time shows that decreasing of the gaps is beneficial. Its minimum value is limited by the longitudinal compass displacement in inhomogeneous fields (in gaps between solenoids) and by cart rotations (see Section 4.5).

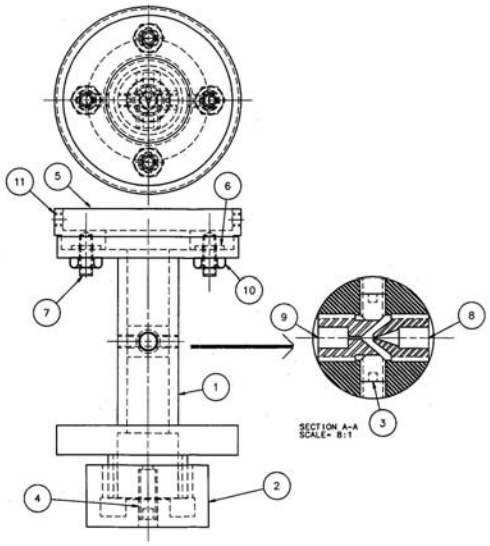

Figure 5 Compass design: 1 – field sensor body; 2 – balancing nut; 3 – wire fixing screw; 4 – balancing nut locking screw; 5 – mirror adjuster; 6 – four spring lock washers; 7 - four mirror adjustment screws; 8 – wire clamp adjustment screw; 9 – wire clamp; 10 – four mirror adjustment nuts; 11 - four mirror fixing screws.

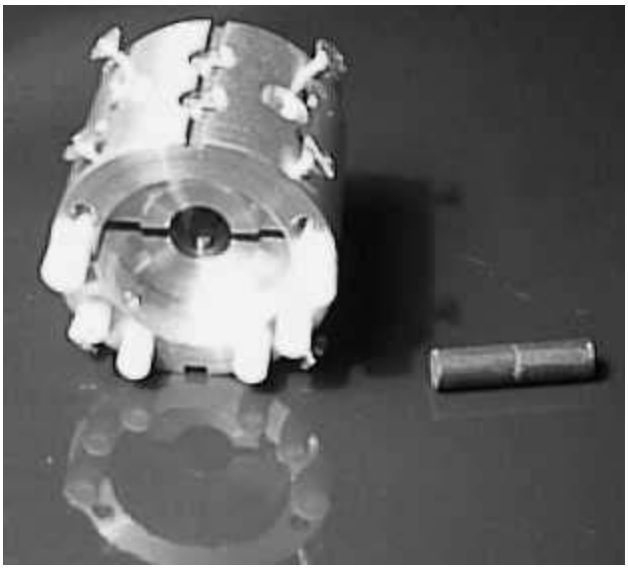

Figure 6 Compass holder consisting of top and bottom halves and two glued NdFeB magnets used as the needle.

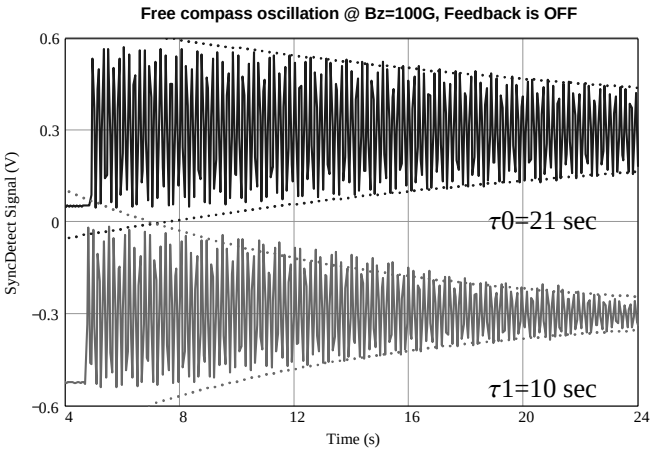

Figure 7 Free compass oscillations and their envelopes when holder bottom half is off (top) and on (bottom). The offsets in +0.3V and -0.3V were applied to top and bottom curves respectively.

Further decrease of the system transition time is done by electronic damping (see Section 3.8); with the closed feedback loop the time is about 4 seconds.

3.4 Optical System

The laser beam, which determines the reference axis of the cooling section, is generated by a laser diode (*Table 2*). Then, the beam is shaped by a focusing system and, after reflection by a mirror and a beam splitter, goes into the solenoid (Figure 4). The total length of the beam path from the laser to the compass mirror to the four-segmented photodiode varies from 10 to 50 m depending on the cart position inside the solenoid; correspondingly, the beam size on the photodiode changes as well. To provide stable and precise measurements, this size has to be well inside the photodiode's active area, 20 mm (*Table 3*). On the other hand, the beam should not interfere with wires guiding the cart and be small enough at the compass mirror. The minimum possible value D_0 of the maximum beam size over the length of L=50 m is determined by a natural divergence of the beam:

$$D_0 \sim \sqrt{L \cdot \lambda} \sim 6 \text{ mm}, \qquad (3.3)$$

where λ= 635 nm is the laser wave length. The beam size is increased to this optimum value by a two-lens expander (Figure 8). An initially elliptic beam is collimated by a round 3.5 mm diaphragm, placed between lenses. The beam convergence angle is adjusted by the distance between lenses (currently d= 225 mm) to achieve the minimum beam size close to the far end of the solenoid. The focal length after the beam expander can be defined as:

$$Focus = \frac{F1 * F2}{F1 + F2 - d} \approx 25.4m \qquad (3.4)$$

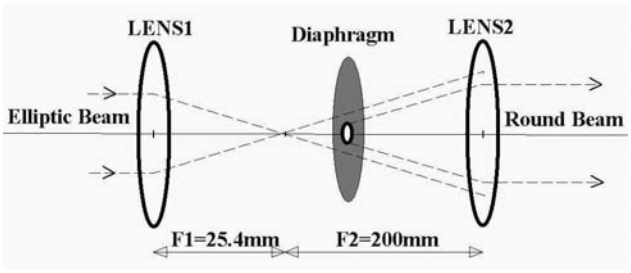

Figure 8 Laser beam focusing. Focal lengths of the lenses LENS1 and LENS2 are 25.4 mm and 200 mm, respectively.

Measurements shown a satisfactory low beam diameter everywhere along its path (Figure 9).

Table 2 HL25MI Laser diode specifications [7]

Parameter	***Value***
Wavelength	635 nm
Max. output power	5 mW
Power stability (better than)	3 %
Divergence	< 0.4 mrad
Beam pointing stability	5 μrad /^{o}C
Modulation bandwidth	5 MHz
Modulation input	±5 V

Table 3 A 4-segmented photodiode specifications [8]

Parameter	***Value***
Active area (4 segments)	Ø20 mm
Elements gap	50 μm
Spectral response range	300-1100 nm
Peak sensitivity wavelength λ_P	720-850 nm
Photo sensitivity S @ $\lambda = \lambda_P$	0.55 A/W
Dark current I_D	< 1.5 μA

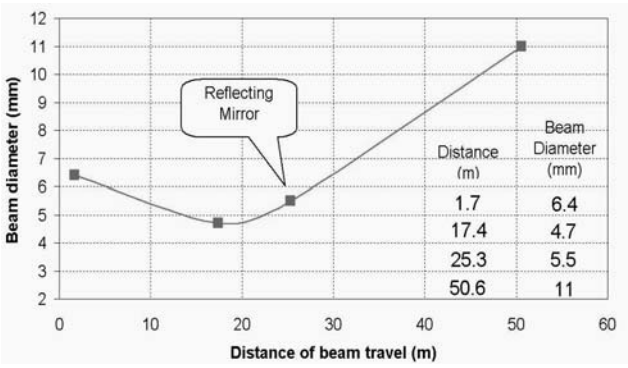

Figure 9 Laser beam diameter as a function of distance.

Figure 10 Kapton film flexible board of compensation coils. Coils on opposite sides (shown in red and blue) provide magnetic fields in two directions.

3.5 Cart Design

The cart transports the compass, the compensation coils and the Hall probe, measuring the longitudinal field component along the solenoid. The cart is made of two materials: aluminum and Teflon (see Figure 11). Teflon-made covers and attachment are the only parts that touch the bottom part of a vacuum tube during cart movements, which is very important for keeping vacuum surfaces as clean as possible.

The shown design provides at least two points of contact with vacuum tube when the cart is traveling through a gap between any of two solenoid modules. It prevents the cart tilting at these critical zones. To prevent the cart from rotation, two titanium guiding wires passing through cart's attachments (marked 3 in Figure 11) are stretched inside the vacuum chamber along the solenoid. The rear side of the cart has a connector to attach a cable powering the compensation coils and the Hall probe.

3.6 Compensation Coils

The compensation coils are flexible boards, printed on a Kapton film. After preliminary simulations in MathCad, the design with two layers has been chosen (Figure 10). Each layer contains one coil that creates fields in X or Y direction. Coil parameters are listed in Table 4. The compass is suspended at the point where the field of compensation coils reaches its maximum.

Table 4 Compensation Coils specification

Parameter	***Value***
Size W x L	119.4 x 169.8 mm
Kapton Thickness	0.3 mm
Number of turns per one winding	39 turns
R_X resistance	14.5 Ohm
R_Y resistance	13.4 Ohm
Z_X impedance @ 1 MHz	74 Ohm / 57^O
Z_Y impedance @ 1 MHz	59 Ohm / 41^O
Calculated Field to Current Ratio (X,Y)	7.615 G/A
Maximum generated field	1.3 G
Field inhomogeneity (I=200mA)	0.1mG

First, the field-to-current coefficient for the compensation coils was calculated and then measured with the precision of ~20% by a Hall probe. The final correction of X and Y coefficients, which takes into account the actual position of the compass in the cart was done by measuring changes in transverse fields induced by the inclination of the solenoid in, respectively, X and Y directions. In a known Bz field, measured by the Hall probe, the inclination by angle $\Delta\alpha$ results in an additional transverse field $\Delta B_{X,Y} = \Delta\alpha \cdot Bz$, which is compared with measured values.

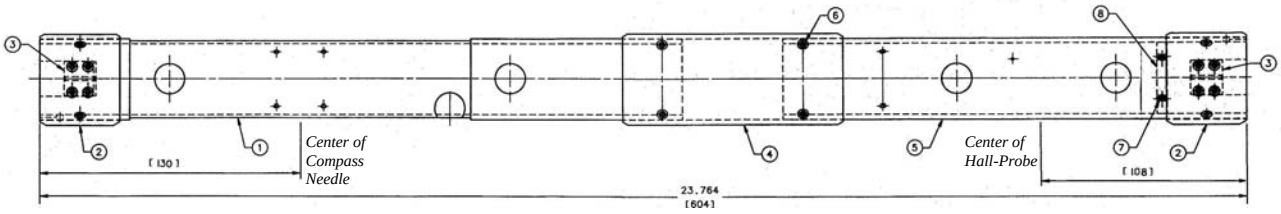

Figure 11 Cart Drawing: 1 – front aluminum body where flex circuit winding (compensation coils) is wound (compass mounted within this body); 2- front and rear Teflon covers; 3 – guiding wire attachment; 4 – Teflon attachment; 5 – rear aluminum body with Hall-probe; 6 – attachment's screw holes; 7 – signal connector mounting holes; 8 - signal connector mount;

The angle, which solenoidal module has with respect to the reference axis of the cooling section can be measured by micrometer gages. On the other hand, this angle can be calculated from the fields measured by compass.

If $\alpha_{M0} = \frac{B_0' - B_0}{B_Z' - B_Z}$ is the X or Y angle, defined by measuring system at two different longitudinal values of B_Z' and B_Z before the solenoid was inclined. And $\alpha_{M1} = \frac{B_1' - B_1}{B_Z' - B_Z}$ is the X or Y angle, defined by measuring system at the same B_Z' and B_Z values after solenoid was inclined. Then one can compare $\Delta\alpha$ measured by micrometers with $\alpha_{M1} - \alpha_{M0}$ and thus calculate field-to-current coefficient.

Namely, if $K = \frac{\Delta\alpha}{\alpha_{M1} - \alpha_{M0}}$, then the actual values of transverse field can be found if the previous filed-to-current coefficient is changed as a factor of *K*.

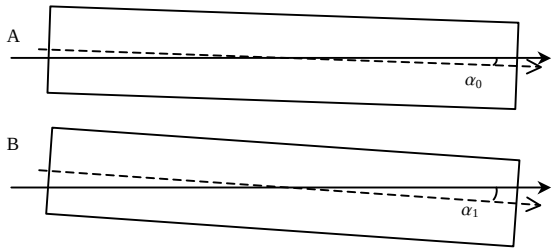

Figure 12 Solenoid placements with respect to laser beam axis (A) – before and (B) after solenoid tilting.

3.7 Transport System

The transport system (

Figure 13) consists of a stepping motor, an encoder, two guiding wires, a pulling string, several pulleys, two limit switches, and signal cable spooler with a servomotor. For better traction, the pulling string is wrapped around stepper motor shaft at the one side of the solenoid and around the encoder shaft at the opposite side. Both ends of the strings are attached to the cart.

The encoder measures the absolute position of the cart in the cooling section with the accuracy of about 1 mm. The direction and the distance of each cart travel is defined by a control program through a stepping motor controller [9].

Maximum cart velocity was programmed to 3 cm/s, which means that a total time for travel the 20 m section without field measurement takes up about 11 minutes. To reduce the cart jerks in the measuring mode the stepping mode controller provides acceleration and deceleration sequences before and after cart reaches its maximum velocity whole traveling between two measurement points. A typical distance between such points was 1 or 2 cm, which took approximately 1 sec for cart to cover. However, the main time consumption during the measurement is not the travel time. After the cart is stopped, a programmed algorithm directs the system to perform the measurement sequence before initiating the next cart travel:

- the time delay for compass oscillations to stop (~10…20 sec);
- turn the feedback on (0 sec);
- the time delay for transient relaxation (~2 sec);
- if the parametric mode used than the time delay to change parameter (~ from 10 to 40 sec);
- turn the feedback off (0 sec);

So, the total measurement time per one point varies depending on the mode used. The values can be between 10 to 90 seconds.

Signal cable spooler

The cable, feeding the compensation coils and the Hall probe, needs an additional handling when the cart travels because the cable has to be reeled either on or off the spooler. The direction and timing of the spooler rotation is controlled by a loop based on measuring of the cable vertical position (the sag) in a space between the vacuum tube and spooler servomotor (

Figure 13). The information about the sag is read by a set of optoelectronic couples.

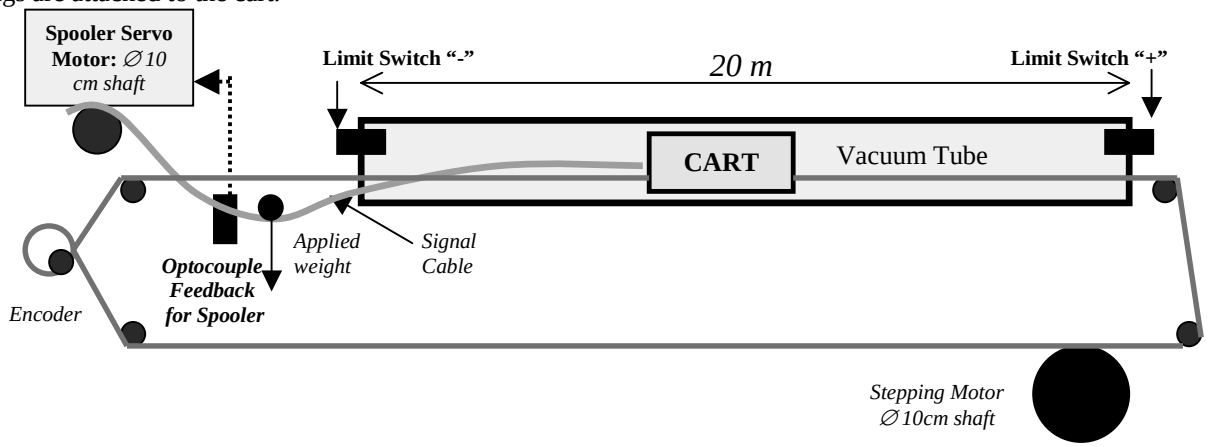

Figure 13 Layout of transport system (guiding wires not shown).

When the cart moves in the positive direction, to the stepping motor, the cable is drawn into the vacuum tube. As a result, the sag becomes smaller, and finally the cable crosses the uppermost optocoupler. The optocoupler sets a trigger in the feedback schematics, allowing servomotor to reel off a portion of the cable. After the cart stops, the servo keeps rotating until the sagging cable crosses the middle optocoupler. It results in a trigger reset that stops the servomotor.

When the cart travels in the opposite (negative) direction, the schematics works similar but the servo starts rotating oppositely, and the lowermost optocoupler is used instead of the uppermost one. There is one more difference for this direction of motion. Because of a friction between the long cable and the vacuum chamber, the cable doesn't sag enough to reach the lowermost optocoupler. To overcome the friction, an additional weight is applied to the cable in between of the optocoupler box and the solenoid end.

3.8 Electronic Feedback

The electronic feedback system (channels X and Y in Figure 4) is an interface between the compass, which is sensitive to an external transverse field component By(t), and the compensation coil, which generates an oppositely directed field $Bcc(t) \approx -By(t)$. The system has to provide the following features:

- The low-pass filtering to reject signals above 20Hz;
- Rapid transient characteristic to any external step functions;
- An "Infinite gain" for a permanent input "error signal", which means that the field generated by a compensation coil is infinitely close to the measured component;
- A capability to carry out measurements at different values of longitudinal field B_Z = [50…150] Gauss. The field value matters because it changes the compass eigenfrequency as $F \sim \sqrt{B_Z}$ (see Figure 14);

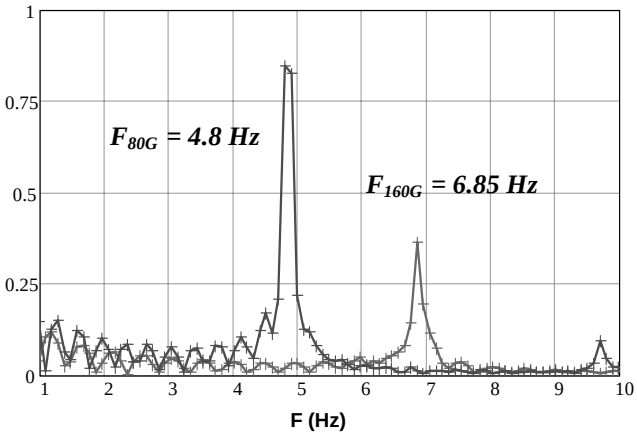

Figure 14 The Fourier transform of compass free oscillations measured at Bz=80G and Bz=160G with the use of synchronous detector after applying a small field distortion of 10mG (similar to shown in Figure 7). $F_{160G}/F_{80G} = 6.85/4.8 = 1.427 \approx \sqrt{2}$, *which is in a good agreement with* $F \sim \sqrt{B_Z}$.

The mathematical simulation (Mathcad and Matlab) of a few prospective schematic possibilities preceded the final feedback design (outlined by dashed line in Figure 15). The simulation was based on a theory of automatic regulation [10], which uses operator form (or transfer function) of linear system differential equations.

To get proper parameters for integrator $W_2(s)$ and differentiator $W_3(s)$, one need to know the exact transfer functions for the Compass' $W_0(s)$, the Compensation Coil' $W_{CC}(s)$ and.the Filter' $W_1(s)$. The following sections describe the implemented approach.

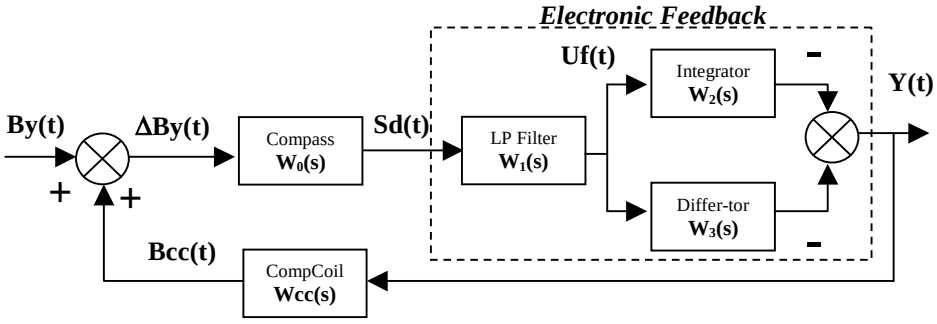

Figure 15 Simplified block-diagram of the measuring system (one of two identical loops for X and Y), where each element is presented by a transfer function.

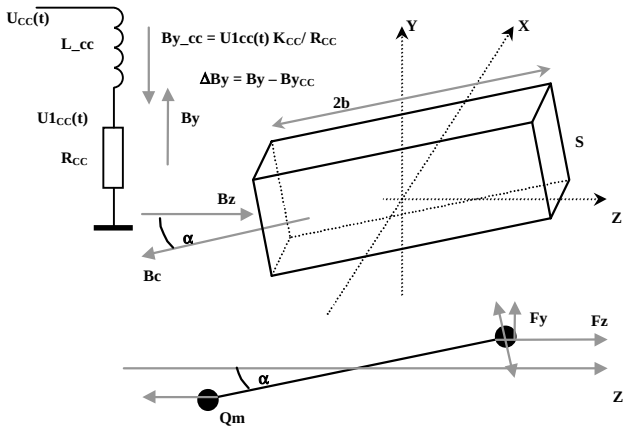

Figure 16 Simulation Model used for definition of Transfer Functions W_{CC} (compensation coil) and W_0 (compass). The permanent magnet used in a compass and shown here as parallelepiped, can be replaced by 2 magnetic monopoles with the charge Qm and mass M.

Filter Transfer Function W_1

The chosen second-order filter is represented by a system of differential equations. After reducing the system to a single equation and applying Laplace Transformation, we have the following transfer function:

$$W_1 = \frac{1}{T_{11}^2 \cdot s^2 + T_{12} \cdot s + 1} \qquad (3.5)$$

where "s" is Laplacian operator.

Integrator and Differentiator Transfer Functions W_2, W_3

The transfer functions for the integrator and differentiator have been already widely described in literature [10], so we used the ones from the tables just providing the right signs and coefficients T_{21} and T_{31}:

$$W_2 = \frac{-1}{T_{21} \cdot s} \qquad (3.6)$$

$$W_3 = -T_{31} \cdot s \qquad (3.7)$$

Compensation Coil Transfer Function W_{CC}

The compensation coil transfer function $W_{CC}(s)$, (responsible for By_{CC} field generation as a result of input voltage U_{CC}) can be found by:

$$\frac{U1_{CC}(t)}{R_{CC}} = -L_{CC} \cdot \int (U_{CC}(t) - U1_{CC}(t)) \cdot dt \ , \text{ or}$$

$$U1'_{CC}(t) \cdot \frac{1}{L_{CC} \cdot R_{CC}} = -(U_{CC}(t) - U1_{CC}(t)) \qquad (3.8)$$

Applying the Laplace Transformation to formula (3.8) gives the following expression:

$$s \cdot U1_{CC}(s) \cdot \frac{1}{L_{CC} \cdot R_{CC}} = -(U_{CC}(s) - U1_{CC}(s)) \qquad (3.9)$$

The transfer function is expressed by the relation of the output to the input function, so we have:

$$W_{CC}(s) = \frac{K_{CC}}{R_{CC}} \cdot \frac{U1_{CC}(s)}{U_{CC}(s)} = \frac{K_{CC}}{R_{CC}} \cdot \frac{1}{1 - \frac{s}{L_{CC} \cdot R_{CC}}} \qquad (3.10)$$

Compass Transfer Function W_0

The compass transfer function can be found by applying a current to one of the dipole correctors when compass is placed at the center of the corrector (NOTE: feedback is open!). A field, generated by the current flow in the corrector, kicks the compass, forcing it to oscillate at its eigenfrequency. If the reflected laser beam has been aligned to the photodiode, the induced photodiode signal as a function of time can be used to obtain the values of the eigenfrequency and the damping factor. The normalizing coefficient, K4 (angle to volt), completes the definition of $W_0(s)$.

To find the compass transfer function, $W_0(s)$, we write down the equation of compass oscillation (see Figure 16):

$$J \cdot \frac{d^2\alpha}{dt^2} = -\mu \cdot (Bz \cdot \sin\alpha + By \cdot \cos\alpha) - \gamma \cdot \frac{d\alpha}{dt},$$

where J and μ are the compass moment of inertia and magnetic moment, respectively. The coefficient γ represents the friction. Taking into account that $\alpha << 1$, one can rewrite the above equation as

$$T01^2 \cdot \ddot{\alpha}(t) + T02 \cdot \dot{\alpha}(t) + \alpha(t) = K4 \cdot B_Y(t), \qquad (3.11)$$

where $T01 = \sqrt{\frac{J}{\mu \cdot B_Z}}$, $T02 = 10\,\text{sec}$, $K4 = -\frac{1}{B_Z}$.

The value of time constant, T02, was estimated from the measurements presented in Figure 7.

After the Laplace transformation, the transfer function is as follows:

$$W_0(s) = -\frac{K4}{T01^2 \cdot s^2 + T02 \cdot s + 1} \qquad (3.12)$$

Simulation Results

After closing the feedback in *Figure 15* one can write now the transfer function of entire system:

$$W(s) = \frac{W_0 \cdot W_1 \cdot (W_2 + W_3)}{1 - W_{cc} \cdot W_0 \cdot W_1 \cdot (W_2 + W_3)} \qquad (3.13)$$

The Matlab simulation of step-like input distortion with By(t)=50mG with properly predefined integrator and differentiator parameters shows that the transient characteristics of the system is less than 2 sec and quite satisfactory for transverse fields measurements (see Figure 17).

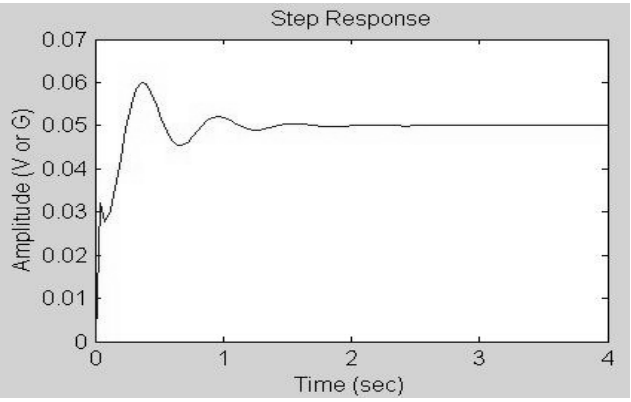

Figure 17 Simulated compensation coil field response as a result of step-like distortion of the external field By.

The measured system behavior for the case of small field distortions is in a good agreement with the characteristics found in simulations. On the other hand, the described procedure of damping of the oscillations works only if the reflected beam is on the photodiode. After moving the cart to a new position, the mechanical perturbation is typically so high that the beam moves outside of the photodiode. Hence, the procedure of measurements includes 12 sec of waiting after each move of the cart with the feedback loop off to allow for the oscillations to be damped "naturally" down to the level when the beam appears on the photodiode, and then the feedback is switched on. As a result, the total time allocated in the control program for oscillation damping is 14 seconds.

3.9 Hall Probe

The Hall probe is mounted in the cart at the far end from compensation coils. It allows carrying out the longitudinal field measurement simultaneously with measurements of transverse components. The Hall probe specifications are presented in Table 5

Table 5 The Hall-probe specification.

Parameter		Value
Wire thickness:	Reference current	0.08 mm
	Hall signal	0.06 mm
Probe size	X x Y x Z	2 x 2 x 0.8 mm
Working zone size		0.8 x 0.25 mm
Resistance	Input	4.2 Ohm
	Output	3.4 Ohm
Max. Power Dissipation		150 mW
Nominal reference Current		100 mA
Offset Voltage		10 μV
Magnetic Sensitivity		6.11 μV/G
Temperature coefficient of Hall voltage		0.0028 %/K
Temperature coefficient of Residual voltage		0.44 μV/K
Nonlinear coefficient at B=2 T		0.42 %
Divergence		-0.003 %
Working Temperature		1.5 … 373 K
B maximum		20000 G

3.10 Measurement Control System

The necessity to measure the solenoid fields at various parameters has required building a dedicated control system. The LabView program running on a PC (see Figure 18) communicates through one serial port with the stepping motor (SM) and through the other with the magnetic measurement controller (MgCnt). To change one of desired parameters during measurements (for example, the corrector or the solenoid currents), the system employs the Linac Classic Protocol to talk to the IRM devices (CXC##, CYC##) or the TCPort protocol to talk to the VAX-server (SPC## which are the Kepco Power Supplies powering the cooling section solenoids). The VAX-server monitors and sets listed devices, contacting Kepcos through the HPIB-controller in the VME module.

One of the important goals for the program is to minimize the number of cart travels along the solenoid to keep the vacuum chamber as clean as possible. It is implemented by adding the "Parametric measurement" option. In this mode, a set of different measurements can be made at each cart position. Typically, two types of parametric measurements are used:

a) Measurements at different Bz values to get solenoid field angles and constant components;
b) Measurement at the different corrector values to determine a cart rotation angle that causes the Bx/By coupling (see Chapter 4.5);

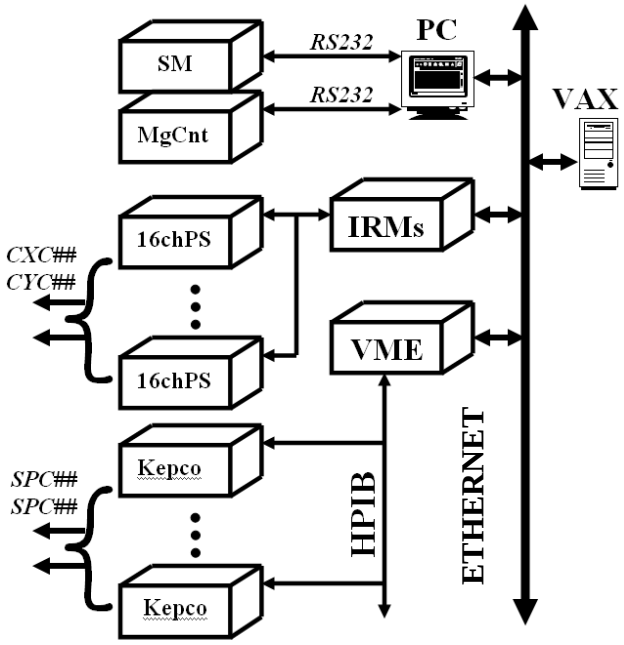

Figure 18 Block-diagram of Measurement Control System. Abbreviations used: SM – stepping motor controller; MgCnt – magnetic measurement controller; PC – Pentium computer with manager program running; 16chPS – 16 channels power supply; Kepco – 100V/10A power supply; IRM – Internet Rack Monitor;

The list of employed libraries:

- MS.LLB: magnetic sensor controller (via serial port COM1);
- MOTION toolbox [11]: Stepping Motor Indexer (via serial port COM2);
- TCPORT: Acnet devices (via Ethernet).
- LinacCP: IRM devices (via Linac Classic Protocol).

4. Measurement Errors Analysis

4.1 Components of Errors

The transverse field B_i (i = x or y), measured by the sensor was always linear with the longitudinal field, $B_z(z)$. The value of $B_i(z)$ consists of several components:

$$B_i(z) = B_{1i} + B_{0i} + \delta B_i = B_z \cdot [\alpha^S{}_i(z) + \alpha^L{}_i + \alpha^M{}_i] + \\ + [B_i^{Earth}(z) + B_i^{Shield}(z) + B_i^{Sen}] + \delta B_i \quad (4.1)$$

In Eq. (4.1), $\alpha^S(z)_i$ represents imperfections of the solenoid magnetic field; $\alpha^L{}_i$ is the angle between the solenoid axis and the laser beam; $\alpha^M{}_i$ is the angle between the magnetic axis of the compass and the normal to the mirror; $B_i^{Earth}(z)$ is the field, external with respect to the solenoid; $B_i^{Shield}(z)$ is the residual magnetic field of the magnetic shield; B_i^{Sen} is the offset component, originating from misbalance of the sensor, twisting of the compass thread etc.; and δB_i is randomized fluctuations. Here, $<\alpha^S{}_i(z)>= 0$ and $<\delta B_i>= 0$ is chosen zero; <> means an average value in the regular part of a solenoid. Components $\alpha^{S,L,M}{}_i$ proportional to B_z and constants (B_{1i} and B_{0i}, correspondingly) were separated by measuring of magnetic fields at different solenoid currents. The values of α_i^M, B_i^{Sen}, and δB_i represent errors of measurement.

4.2 Statistical errors

When the sensor does not move, scattering of measured fields δB_i is determined by electronics noise and drifts of the laser beam. Figure 19 shows the transverse fields measured over period of 13 hours at constant conditions. Within an hour, typical distribution of errors is close to a Gaussian one with the value of the standard deviation σ_i = 0.3- 0.4 mG. In a longer run, the average values drift significantly. At least partly, it correlates with temperature changes during measurements (see Chapter 4.7).

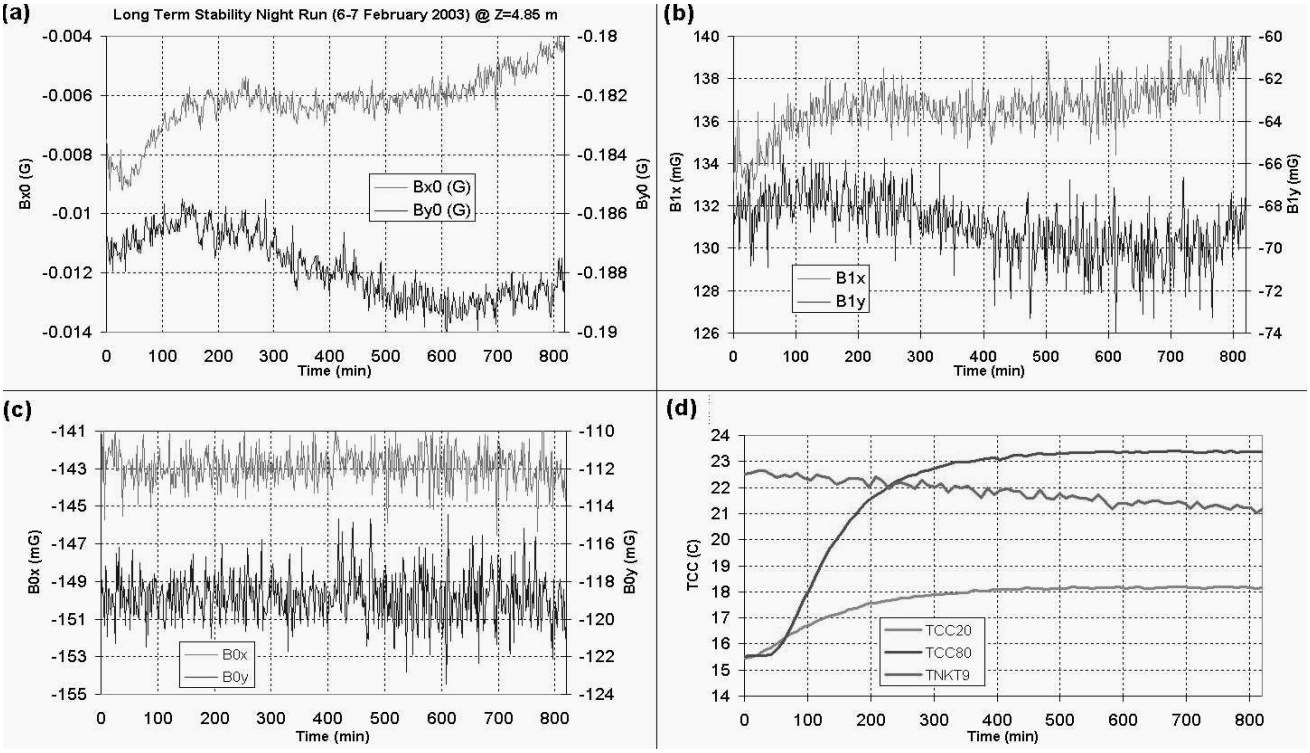

Figure 19 Stability of the measurements when the cart stays at a fixed point Z= 7.82 m. Figures show the measured transverse fields at Bz= 100 G (a), their components proportional to Bz (b), components independent of Bz (c), and temperatures (d). TNKT9 is the ambient temperature, TCC20 is the temperature of the vacuum chamber in the module #2, where the field measurement was being made, and TCC80 is the temperature of the vacuum chamber in the module #8 closest to the laser. The average current was increased in the module #2 at t = 0 and in the module #8 at t=40 min. Temperatures in other modules changed by less than 1.5 C.

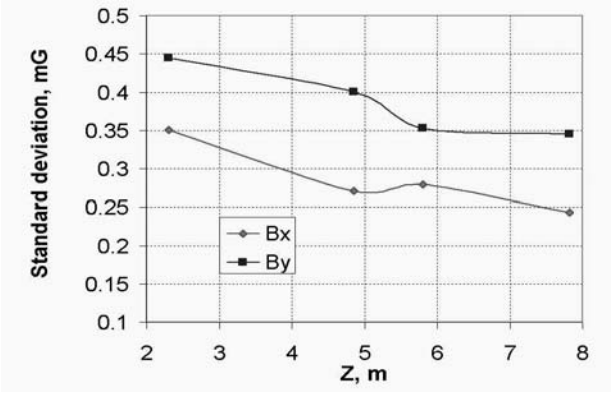

Figure 20 The noise level for the measurements at different locations in the cooling section. Z =0 corresponds to the beginning of the cooling section solenoid (the end farthest from the optical table). Bz= 100 G.

The noise value is slightly larger for locations farther from the optical table (Figure 20). The rate of these changes corresponds to ~0.2 μrad/m and probably reflects the level of air fluctuations inside the vacuum chamber of the cooling section during measurements.

The measurements made with the cart moving along the solenoid show a larger scattering (σ_x = 1 mG, σ_y = 2 mG) and a significant drift of average values (from several mG during hours to 10- 20 mG on a month time scale). For example, Fig. 22 illustrates the difference in values of transverse fields measured at the same settings but separated by a 5-hour interval.. The possible reasons of the increase in the scatter are a cart rotation and changes in a temperature distribution that are discussed in details further in this chapter.

A modified long-term stability measurement, with the feedback being off, is shown in Figure 21. The differential signals SDx and SDy have drifted (~0.4V) while the sum signal of 4 photodiodes (SUM) stayed constant. The temperature conditions changed negligibly (by ~ 0.5^{O}C). To estimate the relation between the induced differential synchronous detector signal (SD_XY) and the altered beam angle we used a Mathcad simulation of SD_XY versus the beam spot size (imaged as a Gaussian distribution with the defined sigma) and the beam offset from the photodiode center (see Figure 22). We found from this simulation, that a 2mm offset corresponds to a 0.08 mrad of the laser beam angle. The latter would give an 8 mG transverse field change for a measurement at Bz=100G, which is quite close to the data we have.

4.3 Systematic errors

Non-zero values of α_i^M and B_i^{Sen} (in Formula 4.1) can result in an incorrect choice of the average values of dipole corrector currents. Also, they increase difficulties caused by cart rotations. Therefore, significant efforts were made to minimize these offsets and their fluctuations.

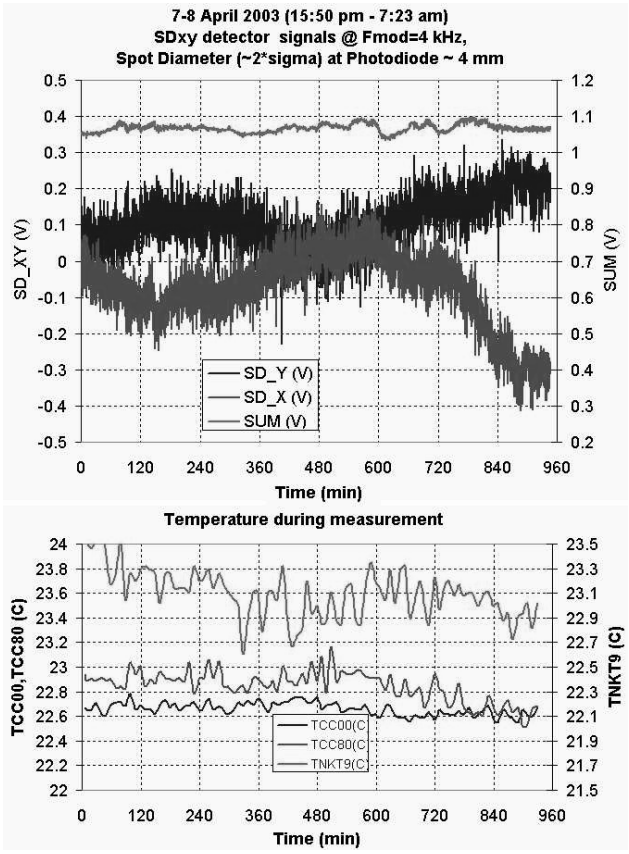

Figure 21 Long-term stability measurement of synchronous detector signals (i.e. when Feedback was off). The 4-segmented photodiode was placed on opposite side of vacuum camber from laser table near Iris2 diaphragm (see Figure 26 for configuration). TCC00, TCC80 are the thermocouple readings placed at the centers of vacuum chambers of solenoid SPC00 and SPC80 respectively, TNKT9 is an ambient temperature of the hall.

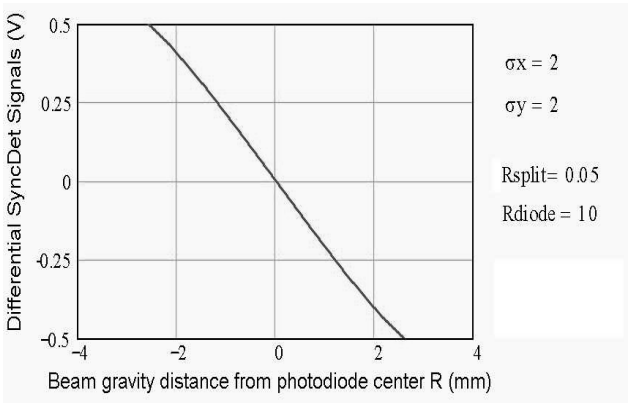

Figure 22 Normalized MathCad simulation for expected induced synchronous detector signal as a function of beam size (sigma) and its position in respect to photodiode center. Synchronous signal change by 0.4V corresponds to ~ 2mm spot shift from the center of photodiode.

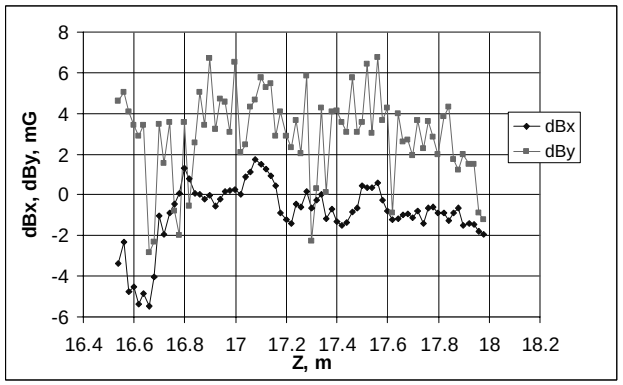

Figure 23 Stability of measurements in the module #8 (the closest to the laser). dBx and dBy are results of subtracting values of, correspondingly, Bx and By fields from those measured at the same settings 5 hours earlier. Bz= 100 G. Average values shifted by 0.9 and 2.8 mG, and standard deviations are 1.5 and 2.2 mG for Bx and By, correspondingly.

Components B_x^{Sen} and B_y^{Sen} shift measured values of transverse fields independently on the longitudinal field strength. They appear because the equilibrium angular position of the compass when the solenoid is off differs from the direction of the laser beam. To rotate the compass toward the direction, additional fields are generated by the compensation coils:

$$B_i^{Sen} = N_i / M_C$$

where $i = x, y$ and M_c is the magnetic moment of the compass. The horizontal component of the torque, N_x, is determined by twisting of the wire that hangs the compass. The twist was dramatically decreased by improving the initial method of fixing the wire. In the current design, shown in Figure 4 (Chapter 3) fixing the wire doesn't involve its twisting or bending so that the resulting B_x^{Sen} can be as low as ~10 mG. *Ny* component of the torque is caused by shifting of the compass center of gravity away from the point of suspension. Position of the gravity center is adjusted by a balancing nut. In the final design, a special attention was paid to provide a good mechanical stability of all compass elements to improve reproducibility. Now in the ten-hours runs the average value of B_y^{Sen} changes by less than 0.5 mG (Figure 19 "C"). Before the improvements were done changes B_y^{Sen} was ~ 100 mG.

In the first sets of measurements, the angle between the magnetic axis of the compass and the normal to the mirror, α_i^M, was found to be surprisingly high, up to 10 mrad. The reason was a large angle between magnetic and mechanical axes of the permanent magnet cylinders. To decrease the value of α_i^M, first, a preliminary selection was performed to avoid magnets with the largest angles. Then, one of two magnets constituting the compass was rotated with respect to the second cylinder to minimize the transverse component of the magnetic moment. Further adjustments were made by mechanical rotation of the mirror plane with respect to the permanent magnet enclosure. When the measured sum $(\alpha_i^M + \alpha_i^L)$ was close to a precision of the solenoid mechanical alignment, a special procedure of compass flipping was used to measure the angle. The compass was rotated by 180 degree around z-axis, and the measurements were repeated. If the compass is not disturbed during this process, α_i^M appears in measured angles with a reversed sign while the solenoid angles α_i^L remain the same; therefore, the value of α_i^M can be calculated from these results. The second rotation by 180° returns the sensor into its initial position. Comparison of α_i^M, measured after this rotation, with the first measurement gives an estimation of reproducibility. In the final compass design the reproducibility was of about ±0.1 mrad while values of α_i^M were below 1 mrad.

4.4 Bx/ By coupling caused by a cart rotation

The guiding wires cannot completely exclude a cart rotation when the cart travels inside the vacuum tube. The rotation results in coupling between measured *Bx* and *By* components because compensation coils rotate together with the cart. The effect is especially pronounced when one of the components is large and doesn't depend on whether the origin of the large value is a solenoid field or sensor errors discussed in the Chapter 4.4

The rotation angle was measured using solenoid dipole correctors. If , for example, the current in a Y corrector changes both components of the transverse field by *ΔBx* and *ΔBy*, the rotation angle is calculated as follows:

$$\varphi = \frac{\Delta Bx}{\sqrt{\Delta Bx^2 + \Delta By^2}} \qquad (4.2)$$

Figure 24 shows results found in two runs at identical conditions. Corresponding rotation angles $\varphi 1$ and $\varphi 2$ behave similarly and differ primarily by a constant value of $\Delta\varphi = \varphi 2 - \varphi 1 = 33 \pm 5 mrad$. Therefore, the cart acquires an angle only entering the vacuum chamber (usually in a ± 50 mrad range) and then travels without significant additional rotation.

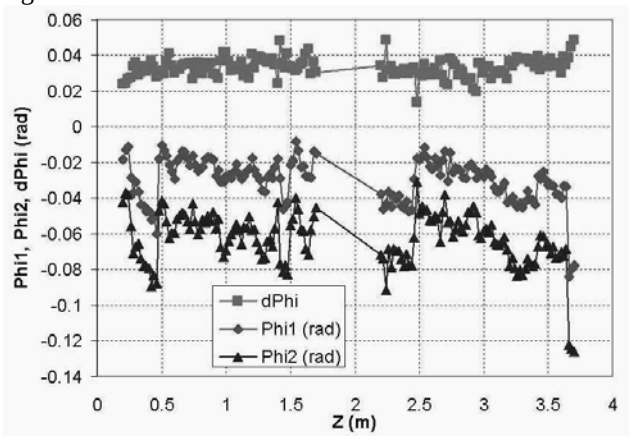

Figure 24 Measurements of cart rotation.

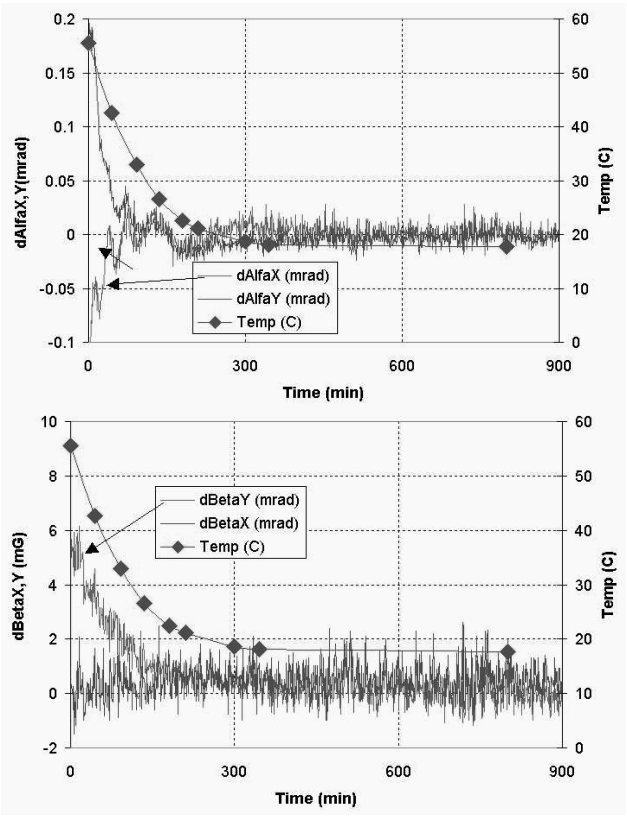

Figure 25 Changes in the measured field components in the time of cooling of a module. The module is SPC80 (closest to the optical table). The sensor is in the center of the module. Heating and cooling of the module was made by switching the cooling water off and on, correspondingly. While heating, the solenoid was run at I= 3.75A, and in the time of measurements the current was kept switching between 2.5 and 3.75 A.

Note that the primary reason for using the compensation coils is decreasing the solenoid field perturbation by proper choice of corrector currents. The better the perturbations are corrected, the lower errors caused by coupling. Hence, the cart rotation increases a number of iterations of corrector currents adjustments but doesn't affect significantly precision of measurements of the final field.

4.5 Errors caused by changes in the sensor temperature

One of the serious problems in the measurements was an unsatisfactory long-term reproducibility. Partly, it was found to be caused by changes of the sensor temperature. Figure 25 shows changes in measured fields when a preheated module was cooled while the compass was positioned in the center of the module. The temperature was monitored by a thermocouple mounted at the center of the module on the outer wall of vacuum tube. Changes in the measured fields approximately follow the temperature.

For the components proportional to B_z, the rates are ~ 5 and ~ 2.5 μrad/K for Y and X, correspondingly; *B0y* rate is ~ 0.15 mG/K, while *B0x* doesn't change. The shift in *B0y* value can be explained by an asymmetrical thermal expansion of the compass that results in a displacement of its gravity center. Drifts of the effective values of the field angles might be caused by several factors. One of them is a thermal deformation of the mirror support that might change the angle between magnetic and optical axes of the compass. Other possibilities are deformations of the solenoid itself and variations in the air refraction coefficient. We suspect that the last explanation is the most probable.

4.6 Laser beam pointing stability

If the laser beam deviates from its "standard" direction in the time of measurements, the feedback system modifies currents in the compensation coils to return the beam into a zero position on the photodiode. In results, it appears as an additional transverse field proportional to B_z (similar for the case of an inclined solenoid). There are several possible reasons for such deviation.

First, the laser itself has a finite stability. In our case, it is 5 μrad/K according to the laser specification (Table 2). After expansion (Figure 8), the stability improves by a factor of F1/F2 =0.127. The room temperature during measurements was typically stable within ±3 K; hence, in a steady state the resulted field error should not exceed 0.2 mG in B_z = 100 G.

Second, refraction in air changes the beam direction if there is a temperature gradient. A simple estimation for an angle $\Delta\alpha$ acquired after passing through a distance z can be made for the case of a static air with a constant temperature gradient dT/dy:

$$\Delta\alpha = \frac{1}{n}\cdot\frac{dn}{dy}\cdot z = \frac{1}{n}\cdot\frac{dn}{dT}\cdot\frac{dT}{dy}\cdot z\,, \qquad (4.3)$$

where n=1.00029 is the air refraction coefficient, and $\frac{dn}{dT} = -\frac{n}{T} \approx 1\cdot 10^{-6}$ 1/K. If one assumes the transverse gradient close to the typical longitudinal one, ~0.1 K/m, the estimation gives $\Delta\alpha$~2 μrad over 20 m length. A real picture is, for sure, much more complicated, and the estimation can give only a guess about the order of magnitude.

Several attempts have been made for better understanding of the errors of this type. Long runs, similar to shown in Figure 19, always demonstrated changes in measured fields when the temperature rose in one of the modules between the compass and the optical table (although amplitude of uncorrelated changes was often comparable). When the measurements were done with switching between two solenoid currents to be able to find B_0 and B_1 components of the transverse field (see Formula4.1), the drifts always appeared as changes in angles B_1 while B_0 stayed unchanged. The results might be explained by motion of the laser light due to refraction in air. The rate of the angle deviation differed considerably from one measurement to another and was within of 2-7 μrad/K.

Also, we made an attempt to estimate a noise of the beam position in a horizontal plane. With the cart being removed, the laser beam coming out of the cooling sec-

tion was focused to a photodiode measuring a total intensity of the light. Then, scrapers mounted in the cooling section at three locations were by turns moved into positions where a scraper crossed the beam pass. Comparison of intensity fluctuations in such half-closed position with those with removed scrapers gives an idea about a beam motion. Fluctuations were higher for scrapers farther from the laser; they were noticeably increasing (~ 50%) when a cover preventing air recirculation near the laser was removed. Unfortunately, a high level of total intensity fluctuations prevented us from getting a good quantitative result. We estimate the beam position fluctuations to be 20-50 μm at the 20 m distance from the optical table (all solenoids were off in the time of measurements). If the angle rises linearly with distance, the resulting angle fluctuations are ~2-4 μrad and contribute into the magnetic field measurement errors at the level of ~ 0.2-0.4 mG. The latter is close to the value found in measurements.

Finally, position of the beam gravity center of the beam passed through the cooling section was measured as a function of the section's temperature (Figure 26). The beam shifts with the increase of the temperature primarily in the vertical direction (down) at the average rate of 0.34 mm/K. Assuming that the temperature is approximately constant along the cooling section and the shift is determined mainly by air convection between the solenoid and the laser table, the resulting angle is estimated to be ~15 μrad/K. We have no reasonable explanation why the temperature dependence found in the field measurements is several times weaker.

The third possible reason for deviations of the laser light direction is relative mechanical displacements of various optical elements with respect to the cooling section solenoid. After couple-weeks runs, the laser beam, previously aligned in the center of the second reference iris, was typically found there being displaced by 5-10 mm. The beam position in the first reference diaphragm remained unchanged; therefore, the laser beam direction was deviated by 200 –400 μrad. Similar values were found for long-term stability of the field measurements.

Generally speaking, a ground motion can cause displacements of the iris and additional angles in field measurements (see the model in Figure 27). A rough estimation can be made in a framework of "space-time ground diffusion" model, which states that the rms relative displacement Δx (in any direction) of two points located at a distance L (m) grows with time interval T (sec) [12] as follows:

$$< \Delta x^2 >= A \cdot L \cdot T \; ; \qquad (4.4)$$

where A is a site dependent coefficient that is $10^{-5\pm1}\,\mu m^2/(s \cdot m)$. *For* L= *25 m,* T= 10^6 *sec, the estimation gives:*

$$\sqrt{\Delta x^2} = 16 \mu m$$

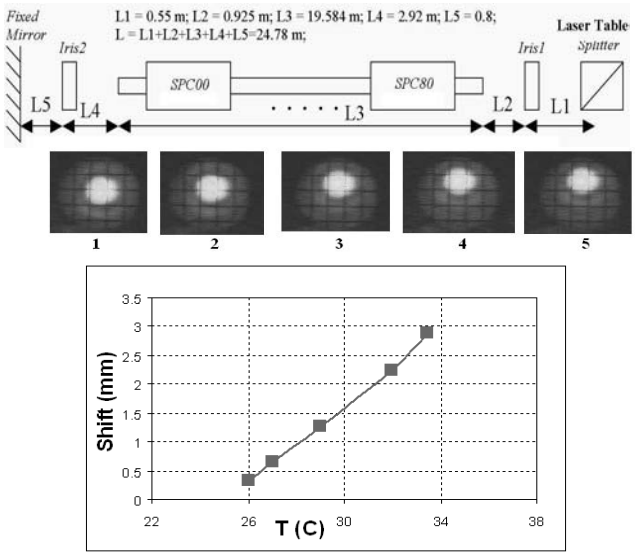

Figure 26 Position of the laser spot on a camera mounted downstream of the cooling section near the IRIS2 as a function of the section temperature. The indicated temperature is an average of readings of 9 thermocouples attached to the vacuum chamber in centers of modules. The data were taken in the time of cooling of the initially heated solenoid. The ambient temperature was 22 ^oC.

and a corresponding angle of α= 0.64 μrad. Obviously, the effect can't significantly contribute into the observed displacement.

Also, the displacements of the laser spot were found when the solenoids were not powered and, therefore, there were no significant temperature gradients. Mechanical distortions of lenses and the optical table support structure seem to be the most natural explanation of the effect.

Note, that these unexplained otherwise drifts were found only in long enough measurements (at least, hours-long, see Figure 19). Typically, measuring of one module took about 1-2 hours. Hence, a slow drift of the laser beam direction results in an incorrect choice of average value of corrector currents in a module. For matching the field lines and an electron beam direction, we anyway will need to adjust the average transverse field in the cooling section, and only misbalance between the averages over module matters. It means, that speeding measurements can alleviate the problem.

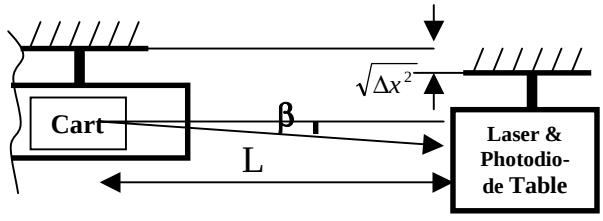

Figure 27 "Ground" or Solenoid Supporting Blocks Motion.

Table 6 Summary of measurement errors

Error	Reason	Characteristics	Typical error value, mG	Effect on final field adjustment
Measurement noise	Electronics noise, air fluctuations	Gaussian	σ_i = 0.2- 0.5	Noise
Constant shifts	Compass misbalance in By	May be adjusted in a well-shielded region	100 - 300	Increase errors caused by cart rotation
	Residual wire twist in Bx		10 - 30	
Constant angle	An angle between magnetic and optical axes of compass	May be adjusted to < 1 mrad according to measurements with flipping the compass	100	Modify the average direction of field lines after adjustment of correctors; increase errors caused by cart rotation
Bx/By coupling	Cart rotation	Rotation angle as high as 0.1 rad; stays inside a module within 10 mrad	10	Make worse measurement reproducibility
Drift of constant By shift	Changes in the compass balance caused by temperature variations	0.15 mG/K	1	Make worse measurement reproducibility
Drift of the laser beam direction	Laser pointing stability	5 μrad/K; 0.6 μrad/K after lenses	0.2	Negligible
	Air fluctuations	~ 4 μrad over 20 m	0.4	Noise
	Refractions caused by air temperature gradients	2-7 μrad/K	0.2- 0.7	Make worse measurement reproducibility
	Mechanical stability of optical elements	200-400 μrad in a month-scale	20- 40	Make worse measurement reproducibility
Bz errors	Hall probe and electronics noise	0.2 G		Negligible

4.7 Summary of errors

Relevant sources of errors are summarized in Table 6.

5. Fields of Solenoids and Correctors

5.1 Influence of Winding Error and Spool Sag

Transverse magnetic fields in the cooling section have several origins. First, manufacturing errors break the solenoid axial symmetry, and a varying transverse field appears in a central part of each module. Further, if a module is inclined with respect to the reference laser beam, let's say, in Y direction by an angle β_y, a transverse field of $\beta_y \cdot B_z$ is added. Third, if the sensor is displaced with respect to the axis of the cooling section, then in the gap between two solenoids the additional transverse field will be measured. In a similar way, if the axes of two adjacent solenoids are shifted with respect to each other, then this shift will create the transverse field in the gap. All these constituents are proportional to B_z. Another part of transverse field is the residual field of cooling section components and the earth field; with a good precision, that part is independent of Bz. Finally, imperfections of the magnetic shield may also disturb the axial symmetry of the solenoid field.

5.2 Solenoid field errors

Solenoid modules were wound around a machined aluminum spool with 6 layers of a square 1.83 X 1.83 mm copper wire. A comparatively thin wire helps to average out short-wavelength field perturbations caused by random tilting of individual turns [13]. The typical length of transverse field perturbations is 0.5 m and is caused most probably by distortions of the spool in the time of solenoid impregnation.

Note that after impregnation the solenoids become stiff enough to withstand the gravity force. To verify that, one of prototype modules was rotated by 180 degree around its axis. Figure 28 shows comparison of transverse fields measured before and after the rotation. The initial shape of the components proportional to B_z is in first approximation a straight line and agrees with an estimation for a parabolic distortion of the solenoid body without impregnation. With a good precision, the fields rotated together with the solenoid, i.e. the shape of winding didn't change.

Regular solenoids were impregnated in a vertical position in attempt to avoid the sag revealed in Figure 29 but it didn't improve the distortions. Magnetic fields, measured in 9 solenoids after correcting the longitudinal field distribution in gaps, are shown in Fig. 26. Typical changes of the transverse components in regular part of modules are < 200 mG at B_z = 100G while in gaps they grow up to 1 G.

Note that in this paper we present preliminary results of measurements in the cooling section prototype that was assembled outside the Recycler ring in a separate building. The final cooling section will consist of 10 modules instead 9 in the prototype, and some changes in the magnetic shield may be implemented.

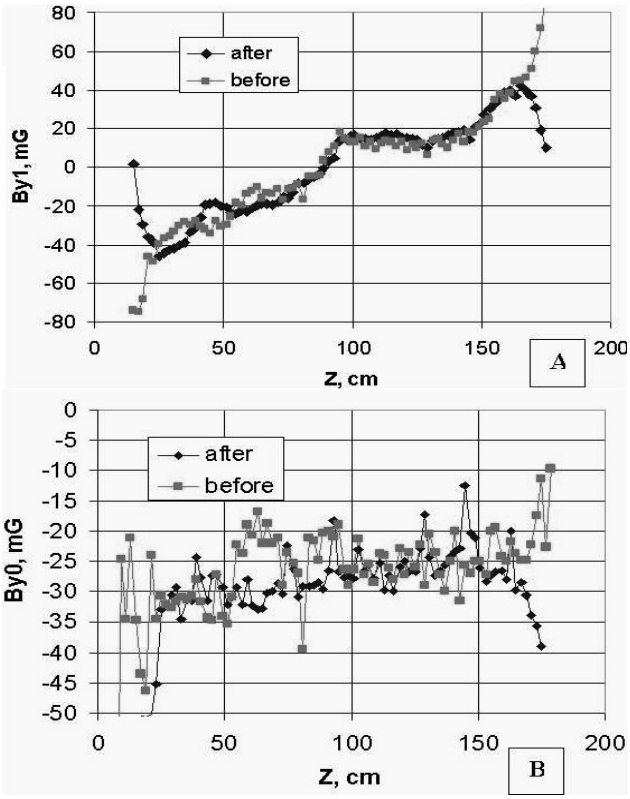

Figure 28 The Y component of a solenoid transverse field, measured before and after a rotation of a module. A and B represent components proportional to B_z *and a constant, correspondingly.* B_z *= 50 G, all correctors are off. Components measured after the rotation are shown with a reversed sign. Average values are fitted.*

5.3 Solenoidal Correctors

To avoid acquiring of transverse velocities by off-axis electron while passing gaps between modules, the longitudinal magnetic field averaged over the gap has to be equal to the field in the regular part of the module. Compensation of the field drop in the gap is made with short solenoidal coils (trim solenoids) mounted on both ends of each module. These trim coils help to compensate the end effects through the instrumentation gaps between two neighbor solenoids.

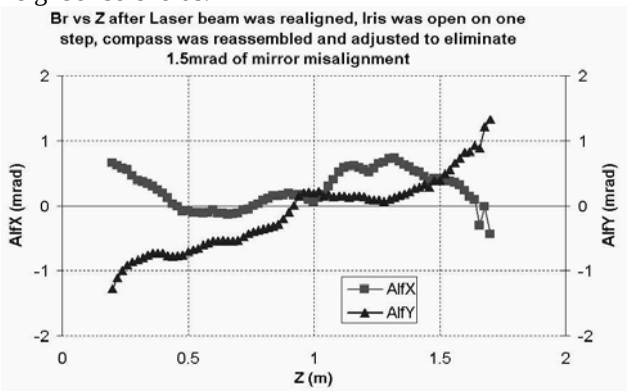

Figure 29 Linear dependence of vertical field component as a result of Solenoidal Sag.

All trim solenoids are powered by a single power supply, and potentiometers connected in parallel to each trim solenoid are used for fine adjustments of their currents. Parameters of the trim solenoids and the longitudinal field distribution are shown in Table 1 and Figure 30.

5.4 Transverse field in the gaps

Transverse fields in the gaps are always significantly larger than in the regular part of the modules. A detailed study performed with two prototype modules showed that partly it is caused by a worse quality of solenoid winding near ends and inclination of trim solenoids. On the other hand, one can consider solenoids near a gap as axisymmetric units whose axes are shifted with respect to the compass position. Indeed, in a paraxial approximation, transverse magnetic field components $\vec{B}_{\perp 1}$ near the entrance of a solenoid is proprtional to the distance $\vec{r}_1$ from its axis. The fields of the solenoid, shifted by Δ, can be presented as a sum of fields of a well-aligned solenoid, $\vec{B}_{\perp 0}$, and a dipole coil:

$$\vec{B}_{\perp 1} = k \cdot \vec{r}_1 = k \cdot (\vec{r} + \vec{\Delta}) = \vec{B}_{\perp 0} + k \cdot \vec{\Delta}, \qquad (5.1)$$

where $k = -\frac{1}{2}\frac{dB_z}{dz}$. If both solenoids, comprising the gap, are shifted with respect to the compass' path, two dipole perturbations contribute into the measured field:

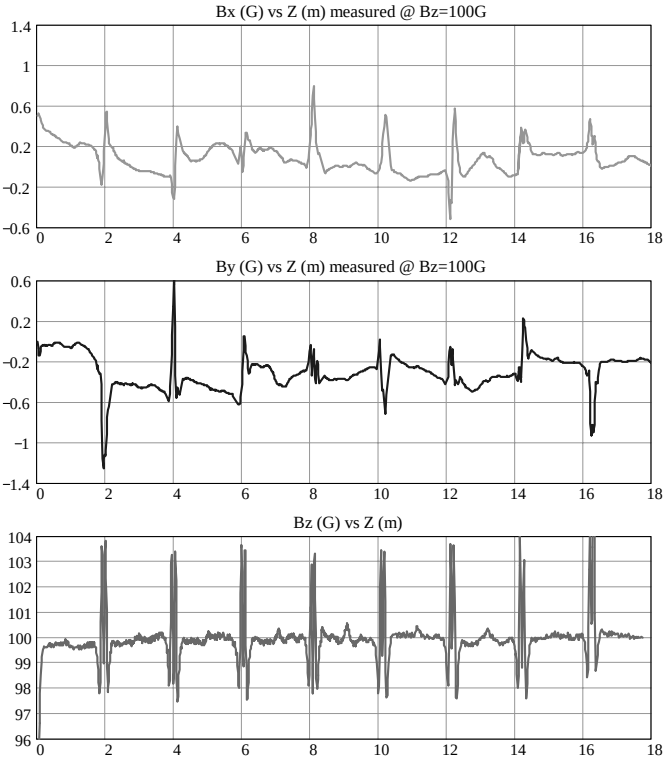

Figure 30 Magnetic Field of 9 cooling section modules measured at Bz=100G (solenoid current of 2.5A).

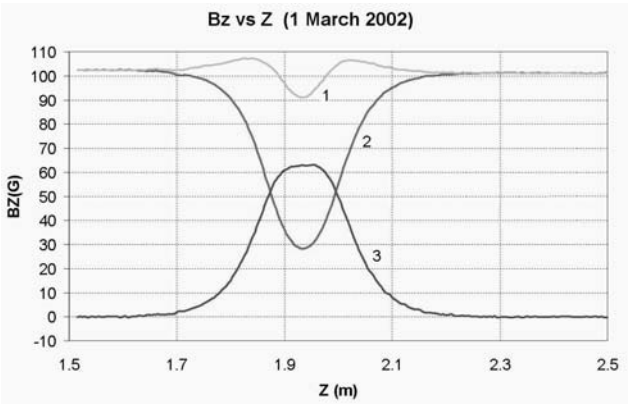

*Figure 31 Typical Trim Solenoids Longitudinal Field (Curve 1: **Bz** vs. $I_{MainSolenoids}$=2.5 A and $I_{TrimSolenoids}$ = 2.45 A; Curve 2: **Bz** vs. $I_{MainSolenoids}$=2.5 A and $I_{TrimSolenoids}$ = 0 A; Curve 3: Difference, Curve1 – Cirve1;*

$$\vec{B}_{\perp} = -\frac{1}{2}\frac{dB^{l}{}_{z}}{dz}\cdot\vec{\Delta}^{l} - \frac{1}{2}\frac{dB^{r}{}_{z}}{dz}\cdot\vec{\Delta}^{r} \qquad (5.2)$$

where indices *l* and *r* correspond to the left and right solenoids.

In the case of the equal shifts (i.e. the sensor is displaced from a common axis of solenoids), the transverse field is proportional to the longitudinal field derivative $\vec{B}_{\perp} = -\frac{1}{2}\frac{dB_z}{dz}\cdot\vec{\Delta}$. The values of B_z are adjusted to be identical in regular parts of the solenoids (Figure 34),and the field integral over the gap is zero:

$$\int_{gap}\vec{B}_{\perp}\,dz = -\frac{\vec{\Delta}}{2}\cdot(B^{r}{}_{z} - B^{l}{}_{z}) = 0\ .$$

Figure 32 shows an example of a field measurement in a gap between two prototype modules. The data shows that B_x component is originated primarily by a sensor displacement, but B_y field is determined by a solenoid shift. In measurements with two prototypes, the gap transverse fields were significantly reduced by alignment of solenoids. In the case of 9 modules, such procedure is more complicated, and in the adjustments described in Chapter 6, compensation of the gap fields was made by dipole correctors installed inside trim solenoids.

5.5 Magnetic Shielding

In the Recycler tunnel where the cooling section will be installed, kA-range Main Injector magnet buses run along the section at a distance about 2 meters. To avoid electron motion perturbations in the time of MI ramps, the cooling section is carefully shielded.

The magnetic shields consist of three cylindrical layers of high permeability alloy that are coaxial with the solenoid magnets. The most important design criterion was effective shielding of steady state and time varying fields in the range of zero to five Gauss. This necessitated a choice of material with high Initial Magnetic Permeability (IMP). IMP is the relative permeability of the material at zero field strength.

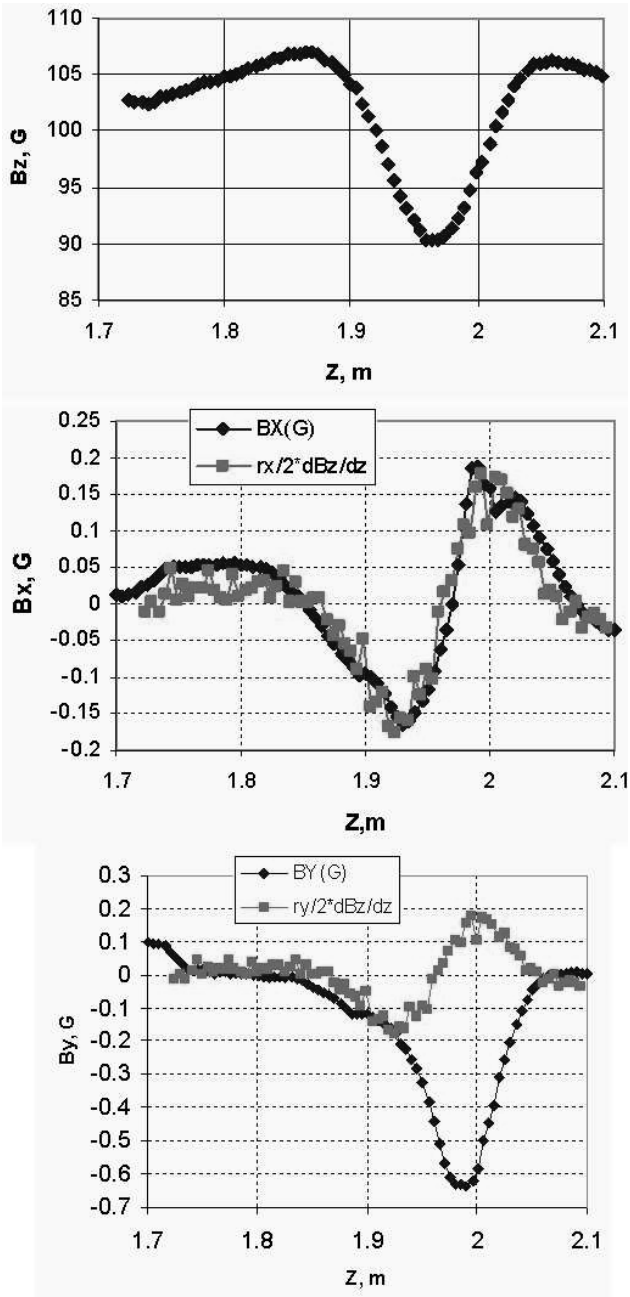

Figure 32 Field measurement in a gap between two prototype modules. Magenta curves correspond to the sensor position shifted by 1.1 mm in each direction.

Table 7 Magnetic Shield specification

Material:	Permalloy 80 (IMP = 40,000 nominal)
Material Thickness:	1 mm
Inner Radius of Layer #1	109.3 mm
Inner Radius of Layer #2	116.7 mm
Inner Radius of Layer #3	133.6 mm

This design does not utilize the mass of magnetic material in an efficient manner, but was driven by the limited amount of inner and outer radial space available for shielding.

Simple analytical calculations and finite element modelling of this geometry agree on a total attenuation factor of 7,400 if the IMP is derated to 15,000. The measured values for attenuation are 4,000 in the vertical direction and 7,000 in the horizontal direction. A lower value for the IMP is to be expected due to inefficiency for longitudinal mechanical joints for the shields (the joints are in the horizontal plane), the result of mechanical stress and shock in handling the shields, and in fastening them together. In order to optimize the IMP, the shields were heat treated by the vendor in a hydrogen furnace after all fabrication was complete.

The shields also function as a flux return for the fields in the 2 Meter Solenoid Magnets. If one assumes the magnets are at their maximum excitation of 150 Gauss, and that the flux is evenly distributed in the shields, the field will be approximately 1,200 Gauss, longitudinal, in the magnetic material. Permalloy 80 saturates at about 7,000 Gauss. This saturation level and the thinness of the material limit the effective shielding in the transverse direction to about 15 Gauss for uniform external fields.

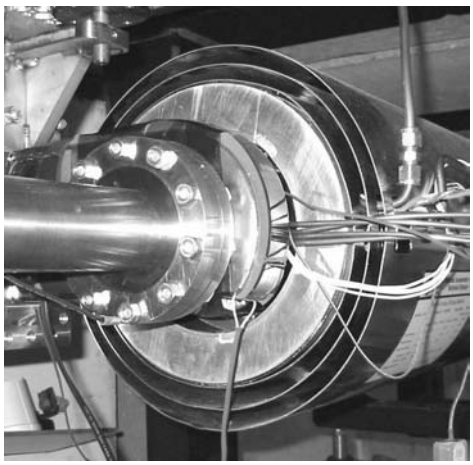

Figure 33 Three layers of magnetic shield.

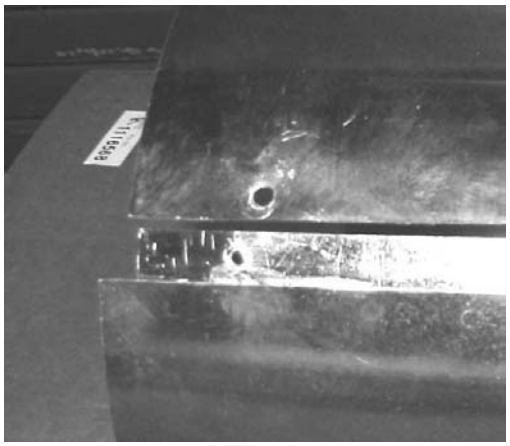

Figure 34 Longitudinal Mechanical Joint.

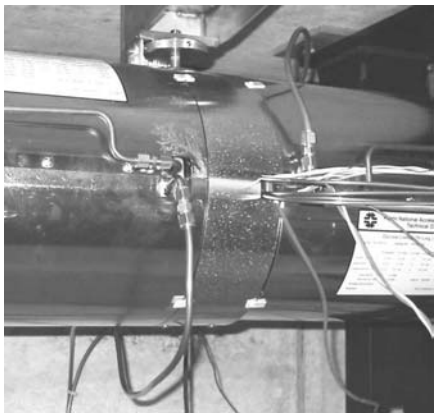

Figure 35 Transverse Mechanical Joint.

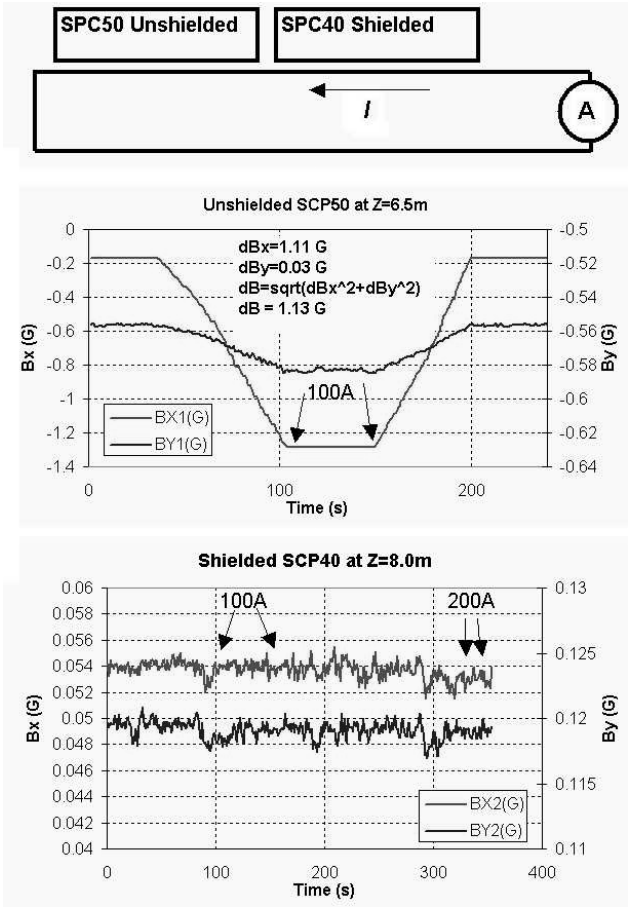

Figure 36 The Measurement of Magnetic Shielding Ratio. SPC40 solenoid had a regular shield, while the SPC50 shield was removed. The wire was stretched along these solenoids at the distance of 19 cm off the solenoid axis. In the measurements the wire current was increased from a zero to 100 A (or 200A). The shielding ratio was found to be higher than 1000.

The longitudinal joints are furnished with a welded overlap plate to lower the magnetic reluctance due to mechanical inaccuracies. The transverse joints in the system, one in the center of each magnet and one at each end of every magnet are simple and imprecise butt joints. In order to minimize perturbations to both the longitudinal

and transverse fields at the centerline of the magnet near these transverse joints, it is necessary to overlay a wrap of 0.15 mm thick Permalloy 80 sheet for each of the three shielding layers. Additional shielding is not required for the longitudinal joints. Some results of shielding ratio measurements are shown in Figure 36 and Figure 37 .

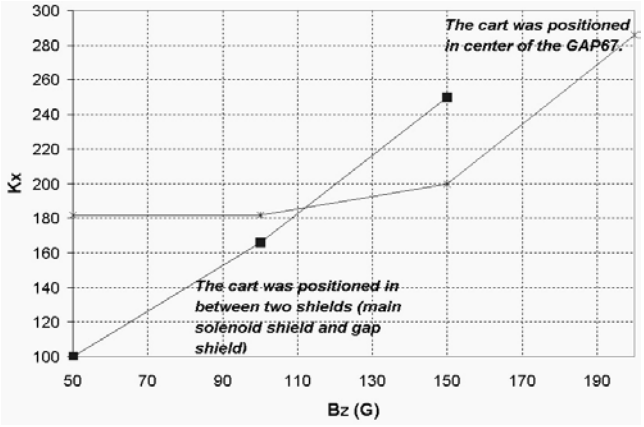

Figure 37 Shielding ratio as a function of longitudinal field measured at two cart positions: a) the cart is in the plane of junction between the main solenoid and gap shields, b) the cart is in the center of the gap67.

5.6 Dipole Correctors

Transverse fields in the regular part of each 2-m module are compensated by 8 identical pairs of dipole correctors. And transverse fields in each gap are compensated by 2 pairs of dipole correctors. The correctors are printed on Kapton flexible boards, which width matches exactly the outside perimeter of the solenoid's outer aluminum tube (Figure 2). Each board carries four coils with opposite coils connected in series. Some parameters of the correctors are specified in Table 1

Distribution of the magnetic field of an individual corrector is close to Gaussian. The field of the correctors installed in the regular part of solenoids complies with the distribution (5.3), while (5.4) holds true for the correctors in the gap:

$$B_{\perp}(z,I)=\frac{0.2\cdot I}{\sigma\cdot\sqrt{2\pi}}e^{-\frac{(z-z_0)^2}{2\sigma^2}} \qquad \sigma=0.09 \qquad (5.3),$$

$$B_{\perp}(z,I)=\frac{0.1\cdot I}{\sigma\cdot\sqrt{2\pi}}e^{\frac{(z-z_0)^2}{2\sigma^2}} \qquad \sigma=0.04 \qquad (5.4),$$

here I is the current fed to the corrector, z_0 is the central coordinate of the corrector. Figure 38 shows the measurements and fit of correctors field.

Figure 39 shows an example of measurements made to calibrate the amplitude of corrector responses.

6. Adjustment of the cooling section field

6.1 Requirements for the field quality

The desired cooling section field quality is determined by necessity to keep electron angles below 0.1 mrad when the electron beam propagates through the cooling section. According to the estimations that take into account electron thermal velocities, aberrations etc., only θ_c~0.06mrad are allowed to be originated by imperfections of the cooling section magnetic field. Electron motion in a measured field can be accurately simulated (see Section 6.3) but for purpose of the field adjustment it is more convenient to use approximate formulas that describe field quality. In Ref. [13] three types of field perturbations were discussed. For the electron energy of 4.3 MeV, magnetic field of B_z = 150 G, and electron offset of 6 mm, there are following restrictions on the field:

1. In a local perturbation of the longitudinal field, an off-axis electron gets an additional azimuthal angle that can be estimated by equation of the generalized momentum conservation ("Busch theorem" for the case of axial symmetry). The angle is below θ_c if

$$\left|\frac{B_z-\langle B_z\rangle_{over\ solenoid}}{\langle B_z\rangle_{over\ solenoid}}\right|<2\cdot10^{-2} \qquad (6.1)$$

2. Even if the amplitude of B_z perturbation is much lower than the limit (6.1) but the perturbation is long enough, an electron can acquire a radial angle. To keep the angle under θ_c, the integral of the B_z deviation over the perturbation length has to be limited

$$\int\left|\frac{B_z-\langle B_z\rangle_{over\ solenoid}}{\langle B_z\rangle_{over\ solenoid}}\right|dz<2 \text{ cm}. \qquad (6.2)$$

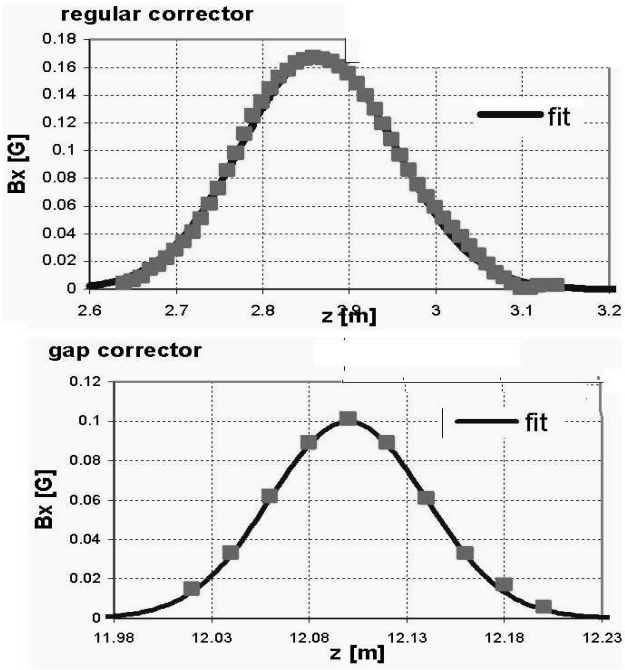

Figure 38 Measurements and fit of correctors field (regular corrector: cor#14, I=0.2A, z_0=2.86m; gap corrector: cor#60, I=0.1A, z_0=12.1m).

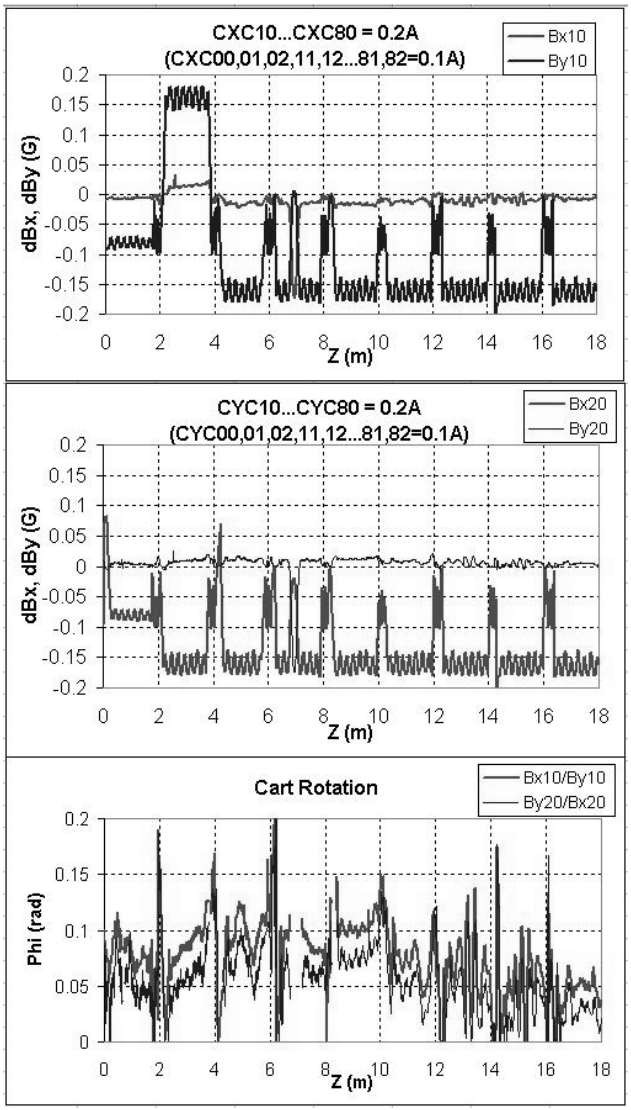

Figure 39 The Measurement of corrector fields (two top Plots) and derivation of cart rotation (bottom Plot).

3. A motion of an on-axis particle is disturbed by dipole field components. For the case when only one of transverse components B_i (i= *X or Y*) is disturbed, the restriction is

$$\int B_i dz < 1 \text{ G·cm} \qquad (6.3)$$

Generally speaking, equations (6.1) - (6.3) are approximations; in part, (6.2) and (6.3) are valid for short perturbations with the length much smaller than the electron cyclotron wavelength (6.7 m for B_z = 150 G). Nevertheless, they give a good estimation for tolerable amplitude of perturbations even for integrals taken over the total length of the section and were used as reference points in the adjustments of the cooling section field.

6.2 Algorithm of Field Adjustment

Field perturbations measured before activation of all correctors were far above restrictions (6.1) - (6.3). Correction algorithm consists of several consecutive steps.

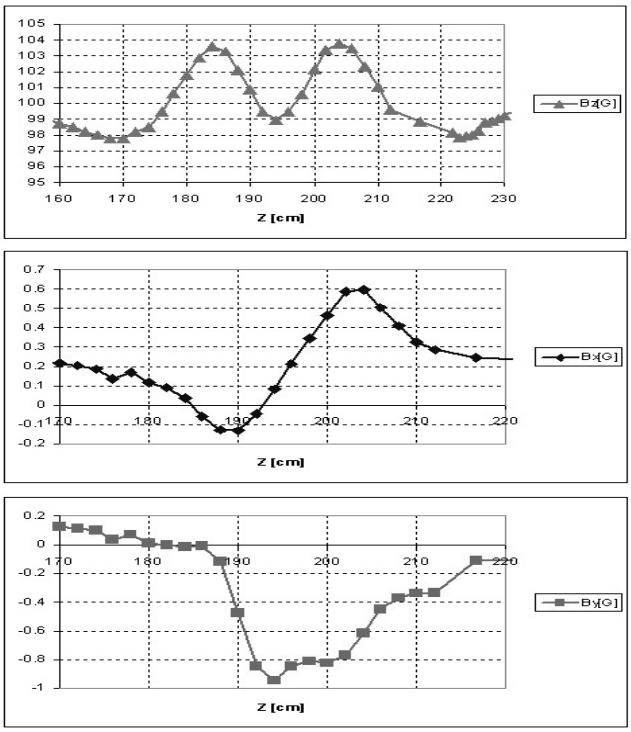

*Figure 40 Fields in the gap between solenoids SPC00 and SPC10. The longitudinal field is compensated in such way that its integral over the gap is less then 0 .1 G*cm.*

1. All solenoids are preliminary aligned mechanically with respect to each other according to the fiducial points positioned at manufacturing on ends of each solenoid.
2. Feeding currents in solenoids are adjusted to equalize the average longitudinal field in each solenoid.
3. Longitudinal correctors are set to correct the longitudinal field in the gaps.
4. Angular positions of modules are corrected according to magnetic field measurements.
5. Transverse fields are compensated by dipole correctors.

6.3 Adjustment of the longitudinal field

After measuring the initial longitudinal field distribution, an average field over the 1.6 m central part of each module was calculated. Relative settings of module solenoid currents were adjusted so that the averages were equal within 0.3%. Because deviations of B_z in regular part of solenoids are less than 0.4%, the contribution of the effect estimated by Eq. (6.1) is negligible.

A typical field distribution in the gap after optimizing the trim solenoid currents is shown in *Figure 40*. Integrals of field deviations over the gap (see Eq. (6.2)) were adjusted down to < 0.1 cm. With this correction, perturbations exceed the limit (6.1) in the gap in the length of 10 cm.

Therefore, after the described adjustments, the longitudinal field disturbances in the gap result in a loss of ~ 5% of the total length of the cooling section for an effective cooling.

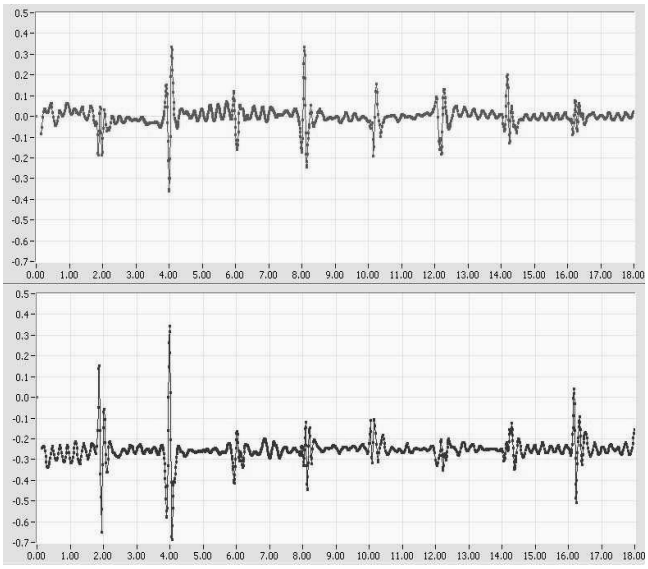

Figure 41 Transversal field measured after compensation.

6.4 Dipole field compensation

Measured field distributions after applying longitudinal field corrections are shown in Figure 41. The average values of measured transverse components are shifted primarily because of compass systematic errors discussed in Section 4.7, which have not been subtracted in these data. Motion of an electron entering the solenoid along the axis with a zero initial angle (in the fields presented in Figure 41 with the compass errors subtraction) was simulated as it is described in Section 6.5. The found values of the total angle

$$\theta = \sqrt{(\frac{v_x}{v})^2 + (\frac{v_y}{v})^2}$$

are shown in Figure 42. The maximum angle is as high as 6.5 mrad and has to be decreased by more than 50 times to be tolerable.

Before describing the field correction procedure, let us note that in this paper we present only preliminary results of field adjustments made in the cooling section prototype. The final measurements and field corrections will be done after assembling of all vacuum elements, that may change mechanical positions of modules, and implementing several improvements into the measurement system.

Transverse field distributions measured before activation of dipole correctors (Figure 30) shown a significant scatter in average angles over modules, ± 2 mrad, left after the initial mechanical alignment (note that first two modules, 0-4 m, have not been aligned). Nevertheless, it was decided, for the sake of speeding up, to skip the step #4 in the adjustment procedure (tilting modules according results of magnetic measurements), and proceed with correcting of the fields with dipole coils.

There are 90 pairs of dipole correctors installed in the cooling section prototype which are constituted by 8 pairs of main dipole correctors, wrapped over the solenoid body, and two trim dipole correctors positioned inside trim solenoids in each of 9 modules. To find corrector settings that minimize transverse field integrals, the whole length of the section was broken into 90 regions ("regions of responsibility" of each corrector), which centers coincide with centers of dipole correctors. Then the integral (6.3) is compensated in every region by the corresponding corrector. The regions are not completely independent one from the other. The fields of adjacent correctors overlap. That means that setting the corrector one should take into account its influence on the adjacent regions.

Taking overlapping into account, the transverse field at coordinate z depends on the currents of all correctors in the following way (please note that in formulas below field is either x or y component of the transverse field, and that currents and coefficients pertain to either x or y correctors respectively):

$$B(z) = \sum_{i=0}^{89} \frac{g(z, z^i_{center}, \sigma_i)}{S_i} I_i \qquad (6.4)$$

where i is the corrector number, g is the Gaussian distribution function (see Chapter 5), and S_i are calibration coefficients (S_i is either 5 or 10[A/G]). Thus, the field integral measured in the n-th region has to be compensated by the corresponding corrector field:

$$\int_{z^n_{left\_border}}^{z^n_{right\_border}} B^{meas}(z)dz = \qquad (6.5)$$

$$= \int_{z^n_{left\_border}}^{z^n_{right\_border}} \sum_{i=0}^{89} \frac{g(z, z^i_{center}, \sigma_i)}{S_i} I_i dz$$

z_{left_border} and z_{right_border} are the borders of the n-th region and B^{meas} is the measured field.

Equations (6.5) form a system of linear equations with respect to corrector currents:

$$\sum_i A_{ni} I_i = C_{n,}, \qquad (6.6)$$

where each matrix coefficient A_{ni} represents an integral of the field created by i-th corrector in the n-th region (normalized by the corrector current)

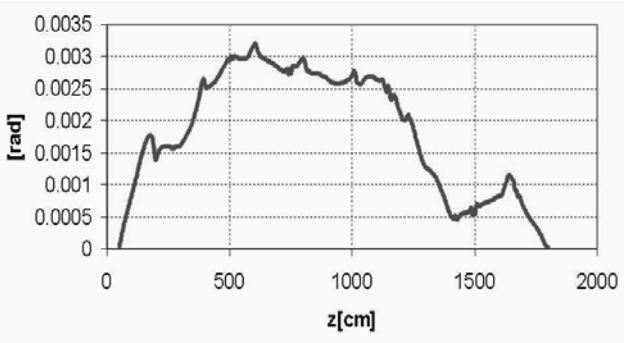

Figure 42 Simulation of the electron motion in uncompensated magnetic field. The average tilt of the solenoid is fitted to provide a zero angle on the solenoid exit (electron enters the solenoid at 5cm off axis).

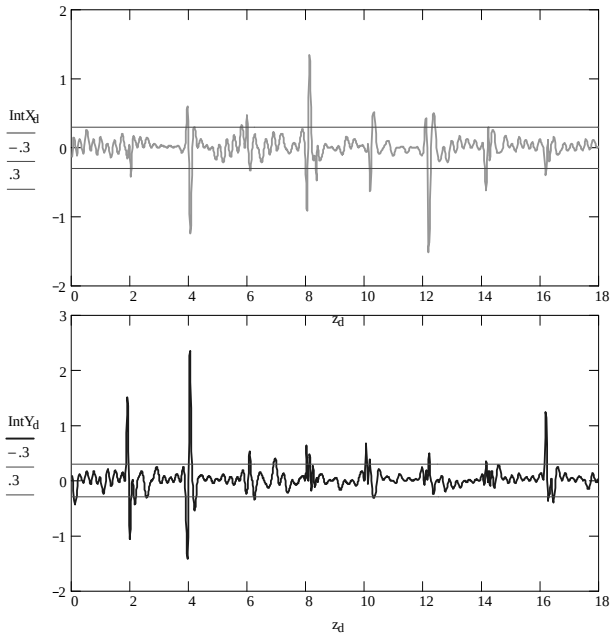

Figure 43 Field integrals expected to be measured after setting all correctors to values found by solving (6.4) with data shown in Fig. 27. The orange lines indicate deviations ±0.3 G·cm.

$A_{ni} = \sum_{i=0}^{89} \left(\int_{z^n_{left\_border}}^{z^n_{right\_border}} \frac{g(z, z^i_{center}, \sigma_i)}{S_i} dz \right)$, and a free term $C_{n,}$ is the measured field integral in the n-th region $C_n = \int_{z^n_{left\_border}}^{z^n_{right\_border}} B^{meas}(z) dz$. The system of equations is bulky (90x90 for each of coordinate), but it is solved easily in MathCad.

The field integrals (6.3) expected after setting all the correctors to optimal value are shown in Figure 43. The requirement (6.1) is fulfilled almost everywhere; moreover, fields in 97% of all section length are within ± 0.3 G·cm. It means that amplitudes of initial field perturbations with sizes smaller than the corrector length are low.

Fields measured after setting all correctors to values found by solving (6.6) are shown in *Figure 44*. They differ significantly from the predicted ones; the integrals deviate up to 10 G·cm. Possible reasons for that are discussed in Chapter 7.

6.5 Numerical Simulation of Electron Motion

Comparison of restrictions (6.1)-(6.3) with measured fields provides only an approximate judgment about the field quality. For more accurate estimation, the motion of an electron in measured fields was simulated.

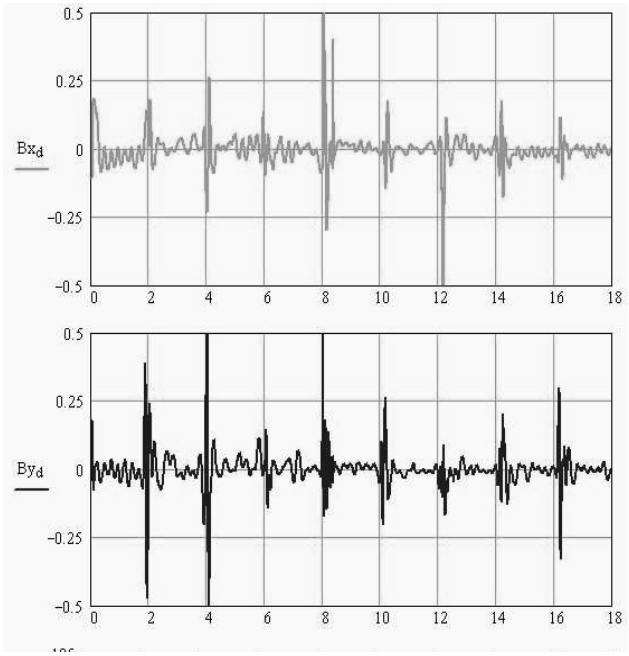

Figure 44 Magnetic fields measured after setting all dipole correctors at values found in simulation.

In the approximation of a constant longitudinal speed of an electron, its motion is described by the following set of equations:

$$\begin{cases} x' = \theta_x \\ y' = \theta_y \\ \theta_x' = \frac{e}{c \cdot \gamma \cdot m \cdot v_z} \cdot \left(B_z \cdot \theta_y - B_y \right) \\ \theta_y' = \frac{e}{c \cdot \gamma \cdot m \cdot v_z} \cdot \left(- B_z \cdot \theta_x + B_x \right) \end{cases} \quad (6.7),$$

where θ_x and θ_y are the angles the electron has with respect to the solenoid axis, apostrophe denotes the $\frac{d}{dz}$ derivative, *e* and *m* are the electron charge and mass, *c* is the speed of light, γ is gamma factor, v_z is the longitudinal speed of the electron, B_x, B_y and B_z are the magnetic field components.

The system (6.7) was integrated numerically with replacing $\frac{du}{dt} + f(u,t) = 0$ by $u^{n+1} = u^n - \frac{1}{2} \cdot (f^n + f^{n+1}) \cdot \Delta t$. This method reduces system (6.5) to the set of algebraic equations, solving which we find:

$$
\begin{cases}
x^{n+1} = x^n + \dfrac{\Delta z}{2}\left(\theta_x{}^n + \theta_x{}^{n+1}\right) \\
y^{n+1} = y^n + \dfrac{\Delta z}{2}\left(\theta_y{}^n + \theta_y{}^{n+1}\right) \\
\theta_x{}^{n+1} = \dfrac{4}{(\alpha\cdot\Delta z)^2\cdot\left(B_z{}^{n+1}\right)^2+4}\cdot\theta_x{}^n + \\
\qquad \dfrac{2\cdot\alpha\cdot\Delta z}{(\alpha\cdot\Delta z)^2\cdot\left(B_z{}^{n+1}\right)^2+4}\cdot\left[\theta_y\cdot\left(B_z{}^n + B_z{}^{n+1}\right) - B_y{}^n - B_v{}^{n+1}\right] + \\
\qquad \dfrac{(\alpha\cdot\Delta z)^2\cdot B_z{}^{n+1}}{(\alpha\cdot\Delta z)^2\cdot\left(B_z{}^{n+1}\right)^2+4}\cdot\left(B_x{}^n + B_x{}^{n+1} - B_z{}^{n+1}\cdot\theta_x{}^{n+1}\right) \\
\theta_y{}^{n+1} = \dfrac{4}{(\alpha\cdot\Delta z)^2\cdot\left(B_z{}^{n+1}\right)^2+4}\cdot\theta_y{}^n + \\
\qquad \dfrac{2\cdot\alpha\cdot\Delta z}{(\alpha\cdot\Delta z)^2\cdot\left(B_z{}^{n+1}\right)^2+4}\cdot\left[-\theta_x\cdot\left(B_z{}^n + B_z{}^{n+1}\right) - B_x{}^n - B_x{}^{n+1}\right] + \\
\qquad \dfrac{(\alpha\cdot\Delta z)^2\cdot B_z{}^{n+1}}{(\alpha\cdot\Delta z)^2\cdot\left(B_z{}^{n+1}\right)^2+4}\cdot\left(B_y{}^n + B_y{}^{n+1} - B_z{}^{n+1}\cdot\theta_y{}^{n+1}\right)
\end{cases}
$$

where $\alpha \equiv \dfrac{e}{c\cdot\gamma\cdot m\cdot v_z}$. This system gives the clear way to calculate the radial displacement and angle of the electron at any coordinate z.

Results of applying the program to data shown in *Figure 44* are presented in *Figure 45* for an electron entering the cooling section with a zero angle and 5 cm radial offset.

Though the resulting electron angle has been decreased by an order of magnitude in comparison with the case of the uncompensated field (Figure 42), it is still much larger than the critical angle.

7. Discussion and plans

When procedure described in Section 6.3 has been applied to two prototype modules, the desirable field quality was demonstrated [14]. Nevertheless, the first attempts to compensate the field in the 18 m solenoid gave more than 8 times larger perturbations. Simulation shown in Figure 43 of the Section 6.4 demonstrates that the quality of uncompensated solenoid field, chosen number of dipole correctors, achieved resolution of measurements, and the algorithm of field correction can provide a satisfactory low level of dipole on 95% of the cooling section length. Measurements with an optical alignment equipment shown a good mechanical stability of modules. Therefore, the difference in results between short and long setups is in a poor long-term reproducibility of measurements.

For the illustration we provide Figure 45. It shows the expected and measured magnetic fields in the first solenoid module of the cooling section. The compensation of transverse field was done two weeks later the measurements of initial field were done (of course the settings for the correctors were calculated and the predictions for compensation were done on the bases of initial measurements). Predicted and measured compensated fields are slightly shifted with respect to each other, what proves the theory of long term instabilities of the measuring system. Even this small shift deteriorates the integral of the field dramatically.

On the other hand if the fields would coincide with predicted ones the angle of electron wouldn't exceed critical angle in the regular part of solenoid. It was demonstrated by simulation (Figure 46).

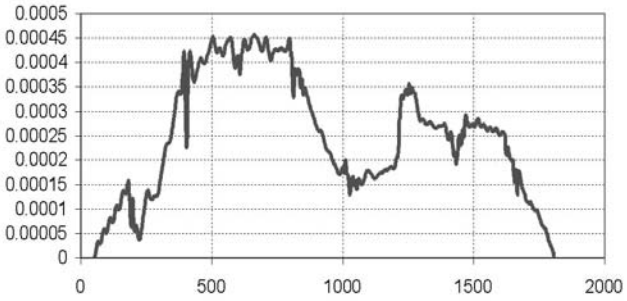

Figure 45 The electron angle simulated in the fields measured after all correctors were adjusted (electron enters the solenoid at 5cm off axis).

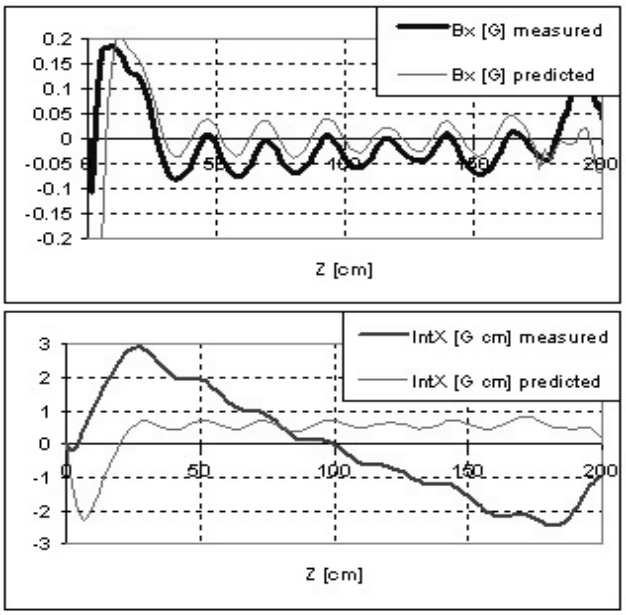

Figure 45 The predicted and the measured transverse compensated fields and their integrals (solenoid SPC00).

Thus we have an effective method of field's compensation. But what has to be done is the improvement of long-term reproducibility of the measurements.

The most important reason for the reproducibility problem in the long solenoid is a combination of an unsatisfactory laser pointing stability and comparatively slow rate of measurements. Because of a jerky start of the cart motion, the compass begins to oscillate with large amplitude. To avoid errors, it is necessary to wait after stopping the card until the oscillations are dumped. As a result, a 2 cm move and a single point measurement take about 17 sec. In gaps, where transverse fields change faster, measurements have to be made even closer, typically, every 1 cm. Totally, the fastest time for measuring of one module is about 40 minutes. Moreover, times for measuring modules farther from the optical table are even larger. Because of air fluctuations, the photodiode signal is noisier; a large laser beam spot size, comparable with the photodiode active region, causes instabilities in the work of the feedback circuitry. Often the computer program was unable to locate the beam onto the photodiode after the card displacement, and it was done manually. The measurement of the complete section required at least two days. In that time, drifts of measured values might be up to 20mG that made chosen corrector settings inadequate. Cart rotation and temperature variations make reproducibility worse as well.

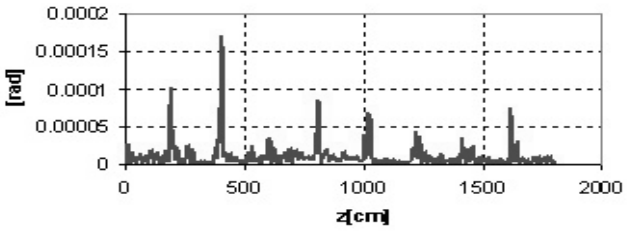

Figure 46 Simulation of electrons motion in the predicted compensated transverse field (electron enters the solenoid at 5cm off axis).

We plan to repeat field measurements after assembling all elements of the cooling section. Several improvements that should decrease the errors are foreseen:

a) the optical table support structure will be made more rigid, and the mechanical stability of all optical elements will be improved;
b) the laser will be replaced by a better one with a fiber coupling to avoid beam astigmatism;
c) the optical system will be improved to use a Gaussian-shaped laser beam with diameter close to 7 mm on the full length of the cooling section;
d) final measurements will be made at a constant temperature over the cooling section;
e) air flow will be restricted by installing shields over the whole laser beam pass;
f) the compass imbalance will be adjusted below 100 mG before measurements;
g) dipole corrector currents will be chosen so that they will compensate measured fields (i.e. a sum of solenoid field plus compass' systematic errors). It will decrease errors due to the cart rotation;
h) the cart design will be improved to speed up measurements and decrease effects of the cart rotation;
i) we will make mechanical alignment of modules according to magnetic measurements to avoid large transverse field in gaps.

In addition, we plan to take care about another type of systematic errors that appears if the center of the photodiode is shifted from the axis of the direct laser beam propagating into the solenoid. The shift modifies the angular position of the sensor's mirror that corresponds to the laser beam being reflected to the photodiode center, and, therefore, results in an appearance of an additional component in the measured transverse magnetic field. Even the error has not been considered in the Section 4, it may be significant and puts restrictions for precision of the photodiode alignment.

8. Conclusion

The future cooling section solenoid has been designed and manufactured; a section prototype consisting of 9 modules was assembled and measured. Simulations show that fields measured in the section prototype can be adjusted with installed dipole correctors to the level suitable for the effective electron cooling.

A compass-based field measurement system demonstrated resolution of 0.2 mG and a short-term reproducibility of several mG. However, an unsatisfactory level of long-term measurement reproducibility, found in the first set of field measurements in a 18-m solenoid, did not allow to compensate the transverse field integral below 10 G·cm. Several improvements proposed to lower the integral to the necessary value of 1 G·cm will be implemented before next set of field measurements.

9. Acknowledgments

Authors are thankful to the members of the Electron Cooling group for their help. J. Leibfritz, A. Makarov, and S. Oplt made the mechanical design of the cooling section; K. Carlson and G. Saewert provided the electrical engineering support; R. Kellet, J. Nelson, and A. Germain assembled the solenoid; E.McCrory proposed one of versions of the transport system; C.Schmidt helped with new design of stable laser table.

Collaboration with Budker INP (Novosibirsk) group was very useful and important. The field measurements became possible due to crucial improvements in the compass-based measurement system proposed by V. Parkhomchuk; the first variant of the compass was developed and produced in INP; participation of V. Bocharov and A. Bubley in measurements of a prototype module was helpful.

REFERENCES

1 Prospectus for an electron cooling system for the Recycler. By J.A. MacLachlan, A. Burov, A.C. Crawford, T. Kroc, S. Nagaitsev, C. Schmidt, A. Sharapa, A. Shemyakin, A.Warner, Proc. of 4th Workshop on the Medium Energy Electron Cooling MEEC-98, edited by I.Meshkov, Dubna, 1999, pp. 25-113

2 A.L.Arapov et al., "Precise solenoid for electron cooling", Proc. of XIII Intern. Conf. on High Energy Particles Accelerators, Novosibirsk, August 7-11, 1986, v.2, pp.341-343;

3 Tim Ellison, PhD Thesis, Indianna University, 1990;

4 M.Steck, L.Croening, K.Nlasche, H.Eickhoff, B.Franczak, B.Franzke, T.Winkler, V.Parkhomchuk, Electron Cooling Assisted Beam Accumulation In The Heavy Ion Synchrotron SIS By Repeated Multiturn Injection, GSI Preprint, Darmstadt;

5 A. Sery, Results of measurements performed at Fermilab' s Electron Lens, private communication;

6 V.N.Bocharov et al, The Precise Magnetic Field Sensor for Solenoids of Cooling Section, Proc. Of XVII Workshop on Particle Accelerators, Protvino, Russia, October 17-20, 2000;

7 http://www.lisalaser.de/tech/hl25spec.html;

8 M.D.Aksenenko, M.L.Baranochnikova, "Optical sensors", Radio I svyaz', Moscow, 1987;

9 Compumotor, 6000 Series Programmer's Guide;

10 V.A.Besekersky, E.P.Popov, The Theory of Automatic Regulation, M. Nauka, 1966;

11 Compumotor, Motion Toolbox User Guide, 1997;

12 B.A.Baklakov,et.al, Preprint INP 91-15, Novosibirsk; Proc. of 1991 IEEE PAC, San-Francisco;

13 S.Nagaitsev, A.Shemyakin and V.Vostrikov, Fermilab-FN-689, April 2000;

14 Field measurements in the cooling section solenoid for the Recycler cooler, by S. Nagaitsev, A. Shemyakin, S. Seletsky, V. Tupikov, Proc. of EPAC'02, Paris, 3-7 June, 2002, p.2373; http://accelconf.web.cern.ch/AccelConf/e02/PAPERS/WEPRI032.pdf;